

Chapter 17

Optical Fiber Sensors for Biomedical Applications

Lee C.L. Chin, William M. Whelan, and I. Alex Vitkin

17.1 Introduction

Optical fiber technology offers a convenient, affordable, safe and effective approach for the delivery and collection of light to and from the tissue region of interest, and has been employed clinically since the 1960s [1]. This chapter discusses and reviews the recent developments in optical fiber sensor technology in the field of biomedicine.

Before proceeding, we distinguish between the previous edition of this chapter (Optics of Fiber and Fiber Probes, 1995 edition, [Chapter 19](#)), which primarily examined the role of optical fibers for *tissue modification* (e.g., photo-therapeutics such as laser heating), and the current treatise. Here, we focus on the clinical application of optical fiber technology for *tissue assessment*, in the contexts of *diagnosis* and *therapeutic monitoring*. While the term *probe* can describe either therapeutic or diagnostic intent, we classify probes for therapy as *applicators* and probes for diagnosis as *sensors*, and limit our discussion to the latter.

The use of optical fiber technology offers numerous advantages that are well-suited for clinical use. The sensors can be made biologically compatible (non-toxic and bio-chemically inert) and are immune from electromagnetic interference. They can be placed *non-invasively* in contact with external organs such as the skin or surgically exposed surfaces. In addition, due to their flexibility and thin outer diameter, they can also be placed into bodily cavities (endoscopic approach), inserted interstitially via minimally invasive trocars, (e.g., hollow bore needles), or positioned intravascularly. As such, measurements can be performed in difficult-to-access parts of the human body with greater “local” sensitivity. Finally, it is technologically possible to bundle multiple sensors with different measurement capabilities into a single probe as a packaged instrument, thus potentially increasing useful information content.

L.C.L. Chin (✉)

Medical Physics Department, Odette Cancer Centre, Toronto, ON, Canada
e-mail: Lee.Chin@sunnybrook.ca

The choice and design of an optical fiber sensor is generally dictated by technological and clinical issues such as access to the target site, spatial resolution, spatial localization, desired sampling volume, (non)invasiveness, accuracy and overall clinical intent. The combination of these factors forms a unique biomedical engineering problem that dictates the various system parameters such as the choice of light source and detector characteristics, source-detector arrangement, and fiber tip modifications, among others. In addition, appropriate signal analysis must be chosen for specific applications (e.g., background fluorescence subtraction in fiber-based Raman spectroscopy, model fits in fiber-based spatially dependent diffuse reflectance, corrections of fluorescence spectra for tissue attenuation distortions, etc.).

In this chapter, the fundamentals of optical fiber sensors will be reviewed, along with basic definitions, classifications and applications. Selected examples are chosen to illustrate the various design concepts. While this chapter by no means constitutes an exhaustive review, we hope to provide the reader with a sampling of the type of approaches and innovations that can be used for solving clinical problems.

17.2 Optical Fiber Sensors

17.2.1 Basic System Design

A typical optical fiber sensing system, shown in Fig. 17.1, is comprised of four major components: a light source, optical fiber(s), optical coupling/filters and a detector.

1. The light source is typically a laser (pulsed, modulated, or steady-state) or white light (xenon or mercury lamp, with or without filters) used to probe or excite

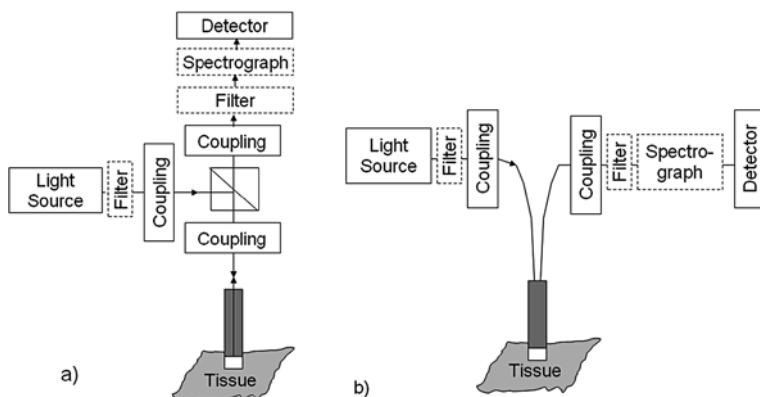


Fig. 17.1 Typical optical fiber sensors employing (a) a single fiber for both delivery and detection or (b) separate source-detector fibers (after Utzinger and Richards-Kortum [2]). Solid boxes represent essential components always present in fiber-based sensor systems; dotted boxes are optical components that may be optimized for a specific application

the tissue. The light source characteristics provide a wide range of properties for optical interrogation of tissues including intensity, phase, polarization state, and wavelength content.

2. Optical fibers deliver light from a light source to a sensing mechanism (see Section 17.2.2 below) located at the fiber end, which is coupled to the interrogated medium (e.g. tissue). Here, the light experiences a *modulation* by the interrogated tissue, and is returned via the same (Fig. 17.1a) or different fiber(s) (Fig. 17.1b) to a light-measurement device where it can be detected and analyzed. Often, a portion of the interrogating light can be used as a reference (the ratio method), to correct for optical fluctuation and to provide improved noise rejection.

Fibers can be bundled to increase the interrogation volume and improve signal-to-noise by capturing a larger signal. This typically requires stripping the outer buffer (jacket) off the fiber to reduce overall diameter. A hexagonal packing configuration provides the optimal arrangement for minimizing the dead space (inactive area between fibers) due to the cladding. The total number of packed fibers, T , in a circular cross section for such an arrangement is

$$T = 1 + \sum_{i=0}^k 6i \quad (17.1)$$

where k is the total number of rings. With the jacket removed, a fiber bundle can achieve a total active area of almost 65%.

3. Optical components such as connectors, lenses, mirrors, fiber couplers, circulators, polarizers, phase modulators, and beam-splitters can be configured to optimize the signal in the detector fiber. Single source-detector geometry results in a small sensor diameter with a small interrogation volume and high light collection efficiency. However, compared to multi-distance sensors and/or fiber bundle geometries, single-fiber sensors suffer from high unwanted background signals generated within the fiber. These can stem from fiber autofluorescence generated by the excitation light or from backscattered illumination light. As such, filters (bandpass, monochromatic) can be used to remove background light or reduce source intensities to appropriate safety levels for both the tissue and the light detection system. Filters can also be applied to the source beam to improve spectral purity and/or to enable spectroscopy.
4. For single wavelength detection and/or spectrally-unresolved total intensity, a photomultiplier tube or photodiode is used, whereas for spectral detection, a charged coupled device (CCD) or spectrograph/monochrometers is used. Conversion of detected light to electrical signal generally requires standard analog-to-digital circuitry.

17.2.2 Classification of Fiber Optic Sensors for Biomedicine

Optical fiber sensors can be divided into two main categories based on the sensing mechanism: *direct* and *indirect*. Direct sensors (e.g., photometric sensors)

utilize the tissue itself to modulate the illuminating light, whereby the collected light is the result of backscattering directly from the interrogated tissue or tissue fluorescence/Raman induced by an optical source. Indirect sensors employ an intermediary in response to the tissue property of interest (e.g., temperature, enzyme presence). Indirect sensors can be subdivided into *intrinsic*, which utilize the fiber itself (core and/or cladding) as the sensing element, and *extrinsic*, which incorporate an additional sensing element at the fiber end (e.g., transducer or substrate). Examples include physical sensors that employ miniaturized transducers that modulate the light in response to such physical parameters as temperature, pressure and radiation dose. Chemical or biosensors evaluate the change in a molecular reagent attached to the end of the fiber via spectroscopic or fluorometric measurement. Such sensors have been utilized for the measurement of pH, glucose, and other intrinsic metabolites. Figure 17.2 presents a diagrammatic overview of the classification schemes for optical fiber sensors in biomedicine.

The primary discussion in this chapter focuses on photonic sensors, since this is the most relevant sensor type in the biophotonics community. Depending on the clinical purpose (diagnostic or dosimetric), *photonic* sensors offer a range of potential modalities that provide unique physical measurements including white light spectroscopy, fluorescence, Raman scattering, optical coherence tomography (OCT), and polarimetry. Of particular importance for sensor design is the choice of the appropriate modality for the given application. Table 17.1 lists the various modalities discussed in this chapter, including an overview of the relevant physical measurements, their advantages and disadvantages, and their potential applications.

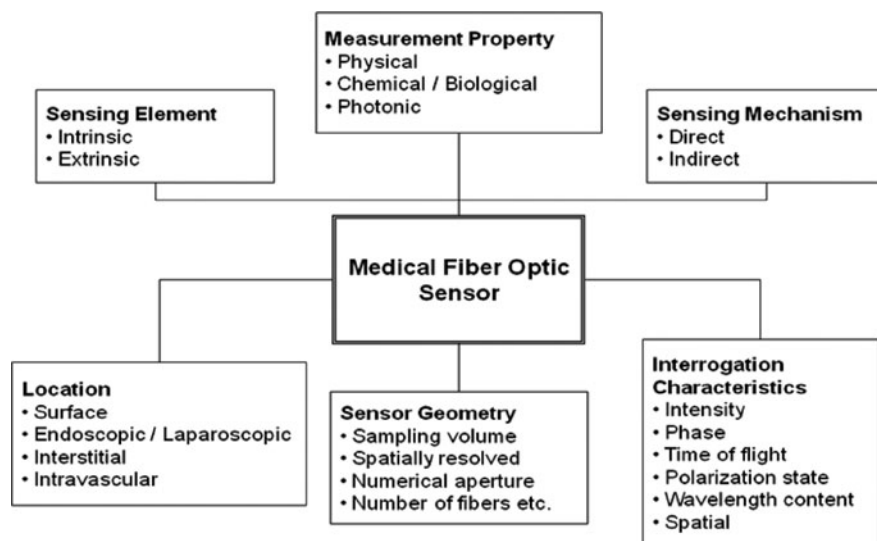


Fig. 17.2 Classification schemes for optical fiber sensors in biomedicine

Table 17.1 Optical fiber sensor modalities to be discussed in this chapter, listing the physical measurements, applications, advantages and disadvantages

Modality	Detection/ determination	Applications	Advantages	Disadvantages
White light spec- troscopy	<ul style="list-style-type: none"> • absolute light intensity • optical properties • chromophore concentration • scatterer spacing and density • oxygen saturation 	<ul style="list-style-type: none"> • diagnosis • oximetry • light intensity dosimetry • chromophore/drug concentration 	<ul style="list-style-type: none"> • range of sampling volumes • relatively inexpensive • potentially simple data processing 	<ul style="list-style-type: none"> • non-imaging • many contributions to the measured signal
Fluorescence	<ul style="list-style-type: none"> • fluorescence intensity • optical properties • fluorophore concentration 	<ul style="list-style-type: none"> • diagnosis • treatment evaluation • fluorophore/drug concentration 	<ul style="list-style-type: none"> • direct measurement • wide array of possible contrast agents 	<ul style="list-style-type: none"> • uncertain sampling volume • auto fluorescence may interfere
Raman	<ul style="list-style-type: none"> • metabolite concentration • optical properties • tissue compositional information • oxygen saturation 	<ul style="list-style-type: none"> • diagnosis • treatment monitoring/evaluation 	<ul style="list-style-type: none"> • high specificity 	<ul style="list-style-type: none"> • weak signals • long(er) integration times • need careful analysis to remove confounding signals
OCT	<ul style="list-style-type: none"> • tissue microstructure • blood flow/Doppler • birefringence 	<ul style="list-style-type: none"> • diagnosis • treatment monitoring/evaluation • tissue functional status (Doppler blood flow maps) 	<ul style="list-style-type: none"> • 3-D imaging 	<ul style="list-style-type: none"> • limited penetration depth

The choice of modality, in turn, guides a specific probe design that must consider the accessibility of the target site. Superficial (exposed surface) tissue can typically be examined using surface reflectance or endoscopic sensors, while internal structures may require sensors suitable for interstitial insertion. Furthermore, in the case of superficial targets, layered structures may require additional design considerations for spatial-depth discrimination. Such factors can be adjusted for using appropriate source-detector geometry and fiber-tip design.

While the specifics of actual sensors will be reviewed, we also examine the physics behind sensor design parameters and their relation to light collection efficiency and sampling volume in turbid media. By focusing on the physics of sensor designs, it is hoped that the reader can extend the information of this chapter to a specific biomedical application.

17.3 Fiber Fundamentals

17.3.1 Light Transmission

A typical optical fiber consists of (1) a central core of refractive index n_1 ; (2) a cladding that encases the core with index of refraction n_2 (with $n_2 < n_1$); and (3) a buffer coating – also known as a “jacket.” The role of the buffer is to improve the mechanical robustness of the fiber and minimize structural compromise from bending. A step-index fiber is shown in Fig. 17.3 which is characterized by a discrete step in the index of refraction at the boundary of the core (n_1) and cladding. Another common design, the graded-index fiber, where the index of refraction decreases gradually from the center of the core to the cladding, and will be discussed later.

When a light ray is directed at the entrance of a fiber with core index of refraction n_1 , a portion of the incoming beam is reflected back into the surrounding medium (index of refraction n_0), while a portion of the beam is transmitted into the fiber according to Snell’s law:

$$\frac{\sin(\alpha_1)}{\sin(\alpha_0)} = \frac{n_0}{n_1} \quad (17.2)$$

where α_0 is the incidence angle and α_1 is the transmission angle into the fiber. Light transport inside optical fibers is based on the concept of total internal reflection, which requires that $n_2 < n_1$ and that the incidence angle at the core/cladding boundary is greater than a critical value, θ_c according to:

$$\sin(\theta_c) = \frac{n_2}{n_1} \quad (17.3)$$

Light rays incident at angles less than θ_c such as at point B in Fig. 17.3 (i.e., more “normal” to the interface) are refracted from the core into the cladding and, hence, do not propagate along the fiber. Now, it is clear from Fig. 17.3 that $\alpha_c = 90^\circ - \theta_c$. Hence, in order to propagate light along an optical fiber, it is necessary to direct light

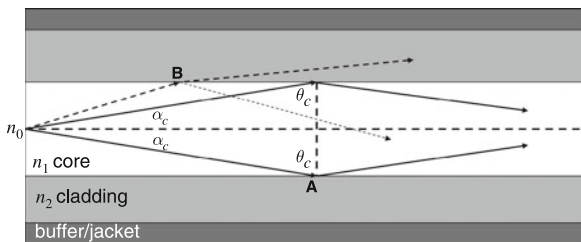


Fig. 17.3 Optical fiber design. n_0 , n_1 and n_2 are the refractive indices of the surrounding medium, fiber core and fiber cladding, respectively. Light rays incident at point A with angles greater than θ_c (Eq.(17.3)) undergo total internal reflection and constitute the propagating light modes; those light rays incident at angles smaller than θ_c (point B) are refracted from the core into the cladding and do not propagate down the fiber. A step-index fiber is shown for illustration (sharp n_1/n_2 boundary)

into the fiber such that it refracts at or below the critical propagation angle, α_c . The maximum angle of incidence that a light ray can enter a fiber and be transported along the fiber (propagate at or below α_c) is known as the acceptance angle, θ_a . For fiber characterization, the acceptance angle is typically reported in terms of a numerical aperture, NA :

$$NA = n_0 \sin(\theta_a) = \sqrt{n_1^2 - n_2^2} \quad (17.4)$$

Hence, for a given acceptance angle, light enters (or leaves) the fiber within an acceptance cone of $2\theta_a$.

From Eq. (17.4), it follows that the NA can be expressed in terms of the refractive indices of the fiber material (core n_1 , and cladding n_2), but is also dependent on the refractive index of the surrounding environment n_0 . As such, compared to an air environment ($n_0=1$), the acceptance angle will be correspondingly smaller in water ($n_0=1.33$). The NA of an optical fiber characterizes not only its ability to collect light from a source, but also preserve the light inside the fiber.

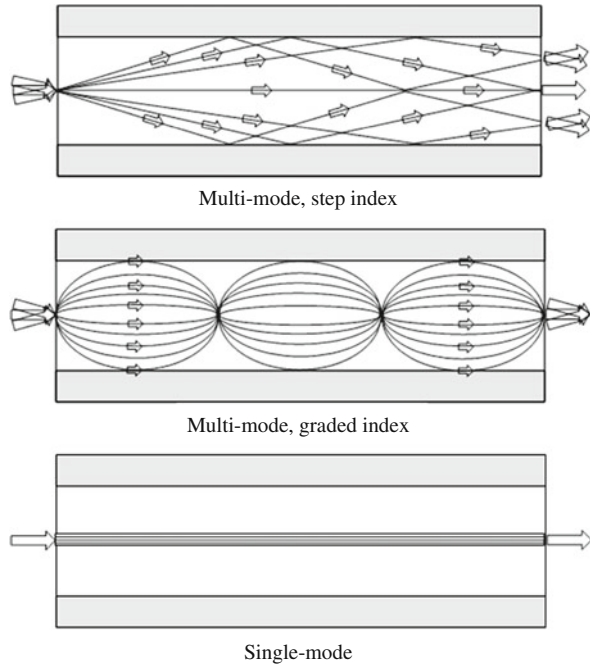
The choice of wavelength range plays an important role in the selection of appropriate core and cladding materials that allow for suitable transmission of light. Conventional glass and plastic core fibers, highly transparent to wavelengths in the visible spectrum, have absorption losses on the order of 0.1% per meter or less. However, optical transmission in the ultraviolet (UV) or infrared (IR) wavelength ranges requires the use of high-grade fused silica cores. In these wavelength ranges, the presence of hydroxyl (OH) radicals in the silica core strongly affects the absorption and transmission characteristics of the fiber. For wavelengths in the UV region ($200 \text{ nm} < \lambda < 360 \text{ nm}$), high-OH fibers are preferred, whereas in the near infrared (NIR) and up to $\sim 2400 \text{ nm}$, low-OH concentration fibers provide the most favorable transmission. In the infrared region beyond $\sim 2400 \text{ nm}$, absorption by silica begins to dominate. In this regime, sapphire fibers provide superior transmission but can suffer additional signal decreases due to high reflection losses at the fiber interface (because of sapphire's high refractive index).

17.3.2 Fiber Classifications

Fibers fall into two broad categories, single mode or multi-mode. A mode is defined as a set of similar paths that light rays travel along the fiber. The term single mode is used to describe a fiber that supports one transmission mode, whereas multi-mode describes a fiber that can support more than one transmission mode. Multi-mode fibers are commonly employed in biomedical applications and come in two basic configurations: step-index and gradient index.

The step-index multi-mode fiber is the simplest design, and operates in the fundamental manner described in Section 17.3.1. Its name comes from the sharp change in refractive index in the fiber material at the core-cladding boundary. In contrast, with gradient-index fibers, the refractive index decreases gradually from the center of the core to the cladding.

Fig. 17.4 Multi-mode (high NA , large core diameter) and single-mode (lower NA , smaller core diameter) fibers



The concept of modes is illustrated in Fig. 17.4. Fibers with a high NA allow light at a large range of incident angles to enter the fiber. The result is that incoming rays with smaller angles of incidence will travel shorter path-lengths closer to the central (optic) axis of the fiber (low order modes), while rays entering at larger incident angles will travel longer path-lengths (higher order modes). Further, impurities in the fiber material of both multi-mode and single-mode fibers can cause leaking at the core/cladding interface. However, due to the longer distance traveled by higher order modes, the effect is enhanced with multi-mode fibers leading to greater transmission losses compared to single-mode fibers.

The number of modes that are transmitted along a fiber is determined by the normalized frequency parameter, V

$$V = \frac{\pi d}{\lambda} NA \quad (17.5)$$

where d is the core diameter and λ is the input wavelength. For step-index and graded-index fibers the number of modes, N_m can be calculated via:

$$N_m = \frac{V^2}{2} \text{ (step-index)} \quad (17.6)$$

$$N_m = \frac{V^2}{4} \text{ (graded-index)} \quad (17.7)$$

Not surprisingly, single-mode fibers typically consist of a small core diameter ($<10\text{ }\mu\text{m}$) and small numerical aperture, while multi-mode fibers have bigger core diameters ($>50\text{ }\mu\text{m}$) and a corresponding larger numerical aperture (0.2–0.4 for silica-core fibers).

When a high coupling efficiency is desired, the optical fiber should have a large NA and the beam spot diameter, d , should be focused such that the focal length, F , of the coupling lens satisfies the condition:

$$F > \frac{d}{2NA} \quad (17.8)$$

However, a large NA results in a larger spectral dispersion of optical pathlengths (since n is typically a function of wavelength) that leads to a degradation of optical information at the distal end through spectral dispersion.

The propagating modes (and hence NA) of an optical fiber are important for both optical coupling efficiency and transmission characteristics. For example, following an initial short (picosecond range) injection of light into a step index multi-mode fiber, the differences in path-lengths among the various modes causes the light to spread out in time as it propagates along the fiber. This temporal broadening of the light pulse is known as modal dispersion, and is an undesirable effect in pulsed light/time-domain optical studies.

To minimize temporal dispersion in multi-mode fibers, a gradient-index design can be employed. Graded-index multi-mode fibers have smaller core diameters (50–90 μm) compared to step-index multi-mode fibers ($>100\text{ }\mu\text{m}$). With graded-index fibers the index of refraction of the core decreases continuously between the central axis and the core-cladding boundary. The index gradient causes light rays to bend smoothly rather than sharply as they approach the core-cladding interface, and allows higher-order modes to travel more in the outer lower-index portion of the core. This effectively reduces the differences in propagation time, thereby reducing temporal modal dispersion.

While graded-index fibers reduce modal dispersion, two other kinds of dispersion still exist: material dispersion and waveguide dispersion. In essence, wavelength-dependent fiber material properties and optical/geometric characteristics of the sensors can cause spatial and/or temporal separation of the different optical wavelengths if a broad-band source is used. Material dispersion arises from the multiple wavelengths present in a laser pulse that result in different refractive indices at each wavelength. This effectively causes each wavelength to travel at different speeds and disperse. Similarly, waveguide dispersion (present in step-index single mode fibers as well) also occurs due to the different wavelengths present in a light pulse. Here, the different traveling speeds are due to core and cladding. Further, the other basic components of the fiber sensor system (Fig. 17.1) also exhibit wavelength-dependent characteristics. These considerations must be taken into account for specific sensor system implementations, especially those employing broad-band sources for tissue spectroscopy with pulsed sources for time-of-flight sensor measurements.

The differences amongst multi-mode and single-mode fibers and step-index and graded-index fibers lead to interesting design considerations when optimizing fiber-optic sensors.

Specific fiber types may be chosen based on dispersion characteristics, transmission capabilities, coupling efficiencies, mechanical flexibility, and biological compatibility, among other criteria.

Since single-mode fibers retain the coherence properties of the input laser light, they are commonly employed for fiber-based interferometers (e.g., OCT sensors). On the other hand, multi-mode fibers with larger NA and core diameter are typically simpler to couple and can transport and collect higher light signals that may be necessary for achieving adequate signal to noise. The choice of appropriate fiber materials must also be considered, to minimize transmission losses for probing tissues at specific wavelengths; while generally not a major consideration in the visible range, this becomes more important for UV and IR fiber sensors.

17.3.3 Fiber Bending

Bending of an optical fiber can lead to light leakage at the area of sharp curvature. When a light ray reaches the fiber bend, higher-order modes that hit the cladding beyond the critical angle leak out of the fiber. Such an effect is less likely for lower order modes. However, low order modes can be converted to higher order modes that then may leak out the fiber at subsequent bends. Although large bends lead to greater light loss, a series of small micro-bends can also lead to a significant decrease in transmission.

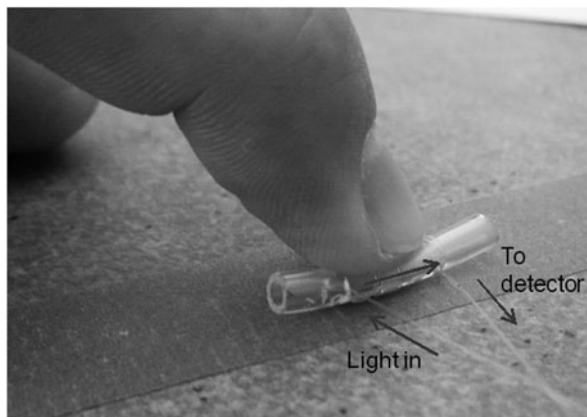
While light loss through micro-bending is generally an unwanted side-effect that leads to signal degradation, the effect can have a number of useful applications. A fiber may be purposely twisted to homogenize and smooth the output beam – also called mode mixing – by converting lower order modes to higher order modes. Similarly, mode stripping is the application of local pressure to optical fibers to modulate the output light patterns exiting a fiber.

Temperature and pressure fiber optic sensors can be constructed to utilize the light loss from fiber bending. Figure 17.5 illustrates a simple micro bending sensor. Optical fibers are positioned between a set of plates with indented groves such that when pressure is applied to the plates micro-bending occurs leading to a decrease in transmitted optical power. Alternatively, the fibers may be encased in a temperature sensitive material which constricts when cooled or heated, again creating light modulation through the resultant change in fiber shape.

17.3.4 Fiber Tip Geometries for Biomedical Sensors

Light exiting or entering an optical fiber can be redirected by sculpting or polishing the fiber tip into a desired configuration. Modified fiber tips are appealing compared

Fig. 17.5 Fiber optic pressure sensor based on light loss from fiber bending. Arrows indicate the direction of light travel. As the finger applies pressure to the tubing, fiber bending results in light loss that is manifested as a loss in detected light signal (from www.sensors.com 2008)



to external optical components for a number of reasons. First, they are more compact and reduce overall system cost by reducing the number of total system components. Second, appropriate tip modification improves optical efficiency, reliability and durability by minimizing the number of optical interfaces (coupling/insertion losses, unwanted reflections), compared to the use of external optics coupled to the fiber end.

A variety of modified fiber tip strategies are available. Implementations that can adjust the spot size and divergence of emitted or collected light and/or steer and direct the beam are all possible. In the following section we briefly review the theory, applications and construction of tapered, ball and side-firing fiber tips. We also discuss the rationale for shielding cap use in tissue.

The described fiber tips are often employed in reflectance sensors to adjust their probing and detection properties, while minimizing sensor size by avoiding the addition of external optics (see [Section 4.1](#)). Spherical and linear diffusers, typically employed in interstitial applications, will be described in [Section 17.4.3.1](#).

17.3.4.1 Tapered Fiber Tips

Tapered (Fig. 17.6b) and ball-lens terminated (Fig. 17.6d) shaped fiber tips increase the light intensity (fluence rate) close to the fiber tip.

Tapered fibers are constructed by increasing or decreasing the diameter of the fiber at either the distal (emitting/detecting) or proximal (laser incident) end. An “up” tapered fiber increases the diameter of the fiber end while a “down” tapered fiber decreases the fiber diameter (see Fig. 17.7).

Tapered fiber optics is governed by [4]:

$$d_1 \sin a_1 = d_2 \sin a_2 \quad (17.9)$$

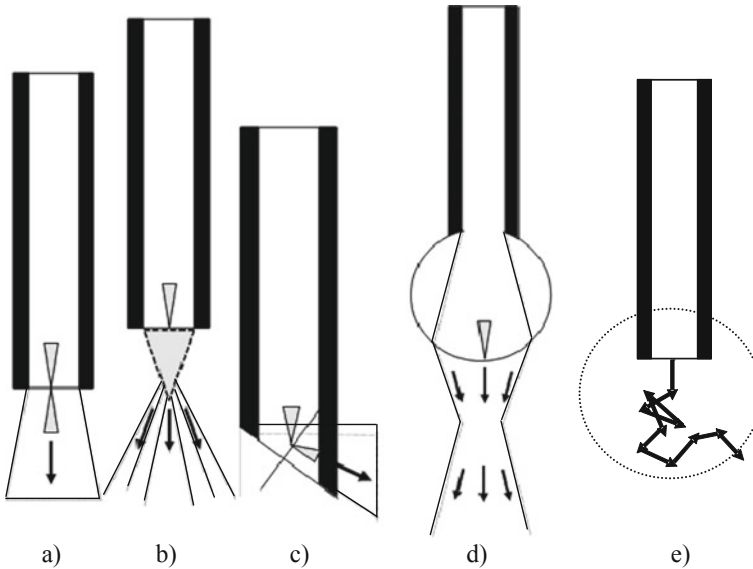


Fig. 17.6 Typical fiber tip modifications (a) plane-cut fiber (b) tapered fiber (c) side-firing (d) ball-lens terminated fiber (e) spherical diffuser. *Small triangles and arrows* are guides for the eye to indicate the direction of light propagation (after Verdaasdonk and Borst [3])

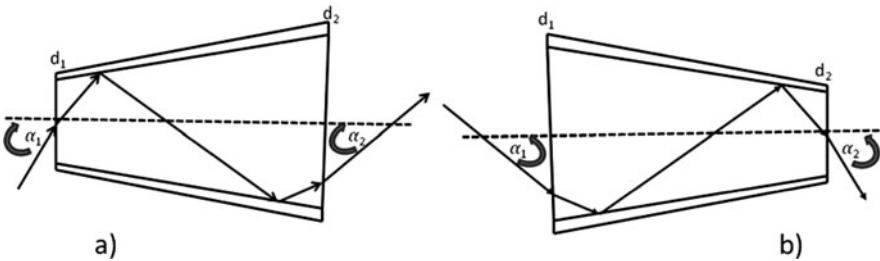


Fig. 17.7 Geometry of incident and reflected rays for tapered fiber tips: (a) up (b) down. The entrance α_1 and exit α_2 angles of the light rays are governed by Eq. (17.9) (after Polymicro Technologies [4])

Light entering the taper will be reflected back and forth with a decreasing (down tapered) or increasing (up tapered) angle of incidence along the taper-length at the core-cladding interface. This will continue until the incident angle of the traveling photons exceeds the critical angle. At this “leaking” point, the photons are refracted out of the fiber. Hence, a “down” tapered tip can be employed to increase the divergence (numerical aperture) while decreasing the spot size of light exiting near the fiber tip. Conversely, an “up” tapered fiber can be used to reduce the NA and enlarge the spot-size of the exiting light. Thus, a down taper tip is a light “spreader” while an up taper is a light “concentrator.”

17.3.4.2 Ball Shaped Fiber Tips

Fiber tips can be also constructed to act as parallel focusing lenses. Such tips include hemispherical elements attached to a plane cut fiber, or ball-shaped endings which are sculpted from the fiber core. The resulting curvature focuses the incoming light rays such that a higher density of light is present near (beyond) the fiber tip (Fig. 17.6d).

A lens bends and focuses light by refracting it. The refraction is accomplished by having different rays pass through different optical thicknesses, thus enabling a lens to focus a (collimated) beam to a (focal) point. Typically, varying optical thickness means a transparent optical element made from a material with a given refractive index n_0 , shaped to have the desired physical thickness profile (e.g., a lens-shape). However, especially when working in confined spaces, it is possible to fix a shape (e.g., cylinder) and have the refractive index vary in a particular fashion, generating the desired “variable optical thickness” effect. Lenses manufactured with this approach are known as GRINs (GRAdient INdex). For example, in the context of fiber optics, cylindrical shaped GRIN lenses with a radially-varying refractive index profile (highest at the centre, dropping off with radial distance, often parabolically, towards the edges) are very popular. Since the end faces of the GRIN lens are flat, relatively straight-forward coupling to a plane-cut termination of an optical fiber is enabled. In this chapter, several optical fiber sensors employ GRIN lenses in their design (see Figs. 17.21 and 17.22).

Alternatively, a fiber tip can be sculpted to a ball shape to adjust beam divergence and spot size and vary the depth of focus of a probing light source. In air, the irradiation properties of spherical tips can be described using paraxial theory [3], which provides an estimation of the position of highest light intensity as a function of the sphere radius.

Paraxial theory predicts that a beam exiting a ball shaped tip in air will be focused to a point at a distance, F_1 , given by:

$$F_1 = R_s \frac{n_0}{n_1 - n_0} \quad (17.10)$$

where R_s is the radius of the ball tip.

A beam with finite diameter (i.e. containing multiple rays) will create an irradiation profile with a “waist”, which is the convolution of “multiple” focal points displaced laterally from the central axis (all also located at also F_1).

Equation (17.10) predicts that for a ball-shaped tip positioned in water, the focal point and region of highest intensity will be located more distally to the ball tip compared to when the ball tip is in air (as n_0 is now greater). In water, the resulting rays are focused so far from the optical axis that the overall beam diameter at F_1 is larger than the beam diameter at the exit surface of the ball tip. This is despite the fact that the individual rays forming the beam profile are still focused distally at F_1 .

In this case, the region of highest intensity is now located between the distal ball surface and F_1 .

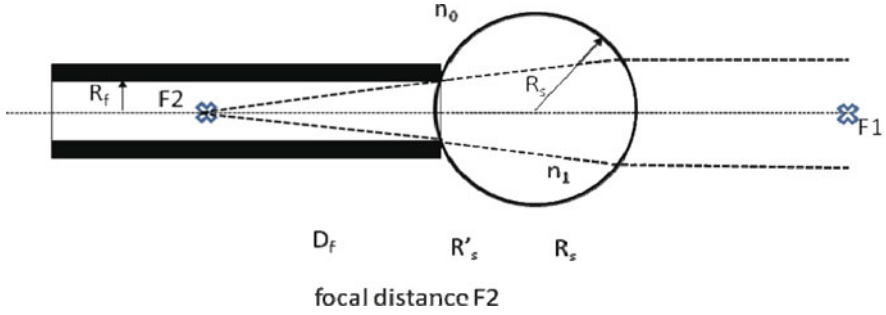


Fig. 17.8 Geometry of ball-lens tipped fiber used in paraxial theory: R_f is the fiber radius, R_s is the ball tip radius, D_f is the distance between the focal point inside the fiber to the end of the fiber, R'_s is the radius of the fiber, $F_2 = D_f + R'_s + R_s$ the proximal focal point, while n_1 and n_0 are the index of refraction of the ball tip and air, respectively (after Verdasdonk and Borst [3])

Paraxial theory can also be used to estimate the conditions under which a converging beam profile is converted into a diverging beam profile. As illustrated in Fig. 17.8, consider a set of rays originating from a point F_2 within the fiber, that converge to a distal focal point, F_1 . F_2 is also known as the proximal focal point. Using geometry, a relationship can be derived from the radius of the ball tip, R_s , the fiber radius, R_f , the refractive index of the surrounding medium, n_0 , the index of refraction of the fiber/ball material, n_1 , and the divergence angle, θ .

From Fig. 17.8:

$$F_2 = D_f + R'_s + R_s \quad (17.11)$$

Here $R'_s = \sqrt{R_s^2 - R_f^2}$ is the radius minus the portion of the ball that is within the fiber itself while $D_f = R_f / \tan \theta$ is the distance from F_2 to the end of the fiber.

Substituting for D_f in Eq. (17.11):

$$F_2 = R_s + \sqrt{R_s^2 - R_f^2} + R_f / \tan \theta \quad (17.12)$$

Paraxial theory states the proximal focal point (located within the fiber), F_2 , is given by:

$$F_2 = R_s \frac{n_1}{n_1 - n_0} \quad (17.13)$$

Inserting Eqs. (17.12) into (17.13) and expanding, we find that the ratio of the sphere radius and sensor is governed by the following relationship:

$$\frac{R_s}{R_f} = T(N - 1) + \frac{\sqrt{T^2 - N(N - 2)}}{N(N - 2)} \quad (17.14)$$

where $N = n_1 / (n_1 - n_0)$ and $T = 1 / \tan \theta$.

The ratio, R_s/R_f , can be used to estimate under what conditions a ball-shaped tip loses its focusing effect. However, it should be noted that the theory is only a first order approximation and ignores the effects of secondary reflections, which can lead to significant deviations. In such cases, ray-tracing provides more reliable predictions of the resulting beam profiles [3].

Both tapered and ball-shaped fiber tips provide a flexible approach for focusing incoming and outgoing light and can be optimized for a variety of applications. These include improving the coupling efficiency with the input laser or other optical components, improving the detection efficiency with a photodiode or photomultiplier tube or, for therapeutic applications, performing high power laser ablation.

17.3.4.3 Side-Firing Tips

Side-firing tips (Fig. 17.9c) redirect the light over a range of angles away from the fiber axis. Side-firing fibers are often employed in therapeutic applications such as photodynamic therapy, thermal therapy, or tissue ablation target scenarios with limited room or maneuverability. Recently, side-firing tips have also been employed as optical sensors for measuring the radiance distribution in turbid media [5, 6].

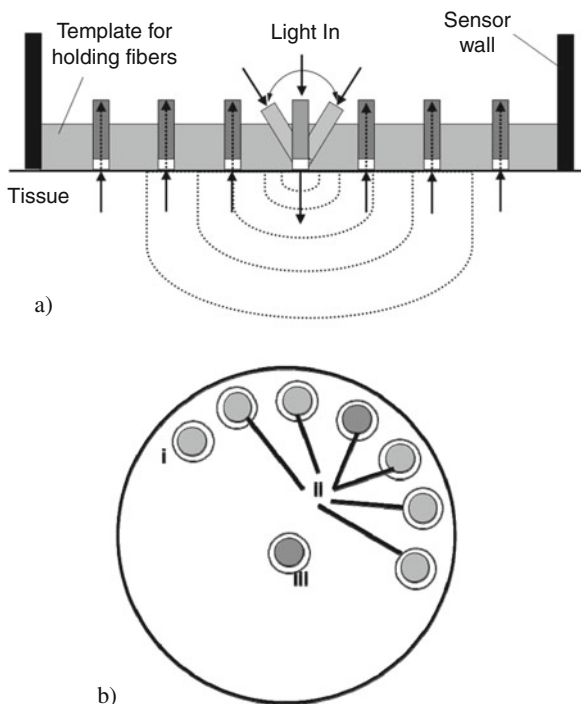


Fig. 17.9 (a) Linear arrangement of reflectance sensors (after Wang and Jacques [9], with permission from Applied Optics) (b) Circular arrangement of reflectance sensors: (i) source fiber (ii) detection fibers (iii) calibration source (after Ref. [10])

An angled-tip with $\sim 10^\circ$ angle can also be used to minimize specular reflection for light-scattering reflectance and/or OCT sensors.

Typically, a side firing fiber with an *NA* of 0.22 should be polished at an angle $>40^\circ$ to ensure total internal reflection. For those light rays reflected at the surface, the exiting beams will be further focused by the curvature of the core, much like a cylindrical lens.

It is important to note that even if the fiber tip is polished at an angle exceeding the angle of total internal reflection, a large portion of rays can still be refracted out the fiber tip. This is because the light traveling within the fiber carries a broad angular distribution such that not all rays can be internally reflected (recall discussion of fiber modes). In addition, when the surrounding environment is water or tissue, the total reflection capabilities of many side-firing tips (calculated with air as the external medium) are lost. In such cases, a transparent shield can be positioned around the tip to allow a surrounding air medium next to the tip, thus preserving its side-firing properties.

Alternatively, right angle micro prisms can be attached, using optical adhesive, to the end of a plain-cut fiber [5, 6]. Here, total internal reflection occurs at the prism's hypotenuse to direct light to/from the fiber. One advantage of this approach is that the prisms can be coated with a thin layer of aluminum to increase the amount of light reflected at the prism hypotenuse (and to capture the off-axis rays that are beyond the total internal reflection condition). Since aluminum is an efficient reflector over a broad range of wavelengths, Al-coated prisms are particularly useful to minimize light leakage in spectroscopic and fluorescence applications. However, the tips can be extremely fragile and typically require a surrounding glass cover to prevent the prisms from being unattached from the fiber during clinical utilization.

17.3.5 Fiber Tip Manufacturing

The majority of the specialized fiber tips described in this section are available via a number of commercial vendors, for example OZ Optics (www.ozoptics.com), Polymicro Technologies, (www.polymicro.com), and LaseOptics (www.laseoptics.com) among others (note that these company names are included for illustrative purposes only, and in no way imply commercial endorsement by the authors) These vendors employ state of the art laser micro-machining equipment for sculpting their fiber tips. However, in-house approaches often offer a more economical and quicker alternative to commercial vendors.

Verdaasdonk and Borst [3] described a simple method for manufacturing ball-shaped fiber tips using a high-temperature burner. Following stripping of the buffer and cladding, a standard silica fiber is exposed to a flame with local temperatures exceeding 2000°C . As a result of the surface tension of the liquid silica, the melted core forms a near spherical droplet that eventually solidifies into a ball-shaped tip.

The authors found that the best approach was to position the flame horizontally with the fiber held beneath the flame at 20–45° from the vertical axis.

A similar approach can be employed to manufacture tapered fibers. Here, the last 1–1.5 cm of the fiber is stripped down to the buffer. The fiber is then positioned in an upside down fashion with a small weight (several hundred grams) attached to the tip. By heating the fiber at the midway point of the stripped region, gravity then draws the molten silica into a taper via the downward pulling weight. The taper angle can be refined by adjusting the fiber diameter, melted volume, and amount of pulling weight. Finally, the taper end is shaped to a point by melting or polishing.

Right-angle side-viewing fiber tips can be created by polishing a plane-cut fiber at an angle equal to or slightly exceeding the critical angle in the medium. In addition, a sputtering machine can be employed to coat the polished surface with a thin, reflecting metal layer (i.e. gold, silver, aluminum) to enhance and supplement the total internal reflection effect.

Finally, shielded fibers can be constructed by encasing the sculpted fiber tips using a clear glass sheath. The glass sheath can be constructed using a glass capillary tube of appropriate diameter by melting the end of the tubing with a flame. The sheath is then attached to the fiber at a location downstream from the tip using a clear UV-cured or chemically cured epoxy, thereby creating an air bubble inside to preserve the tip/air interface.

17.3.5.1 Biomedical Deployment

Combinations of plane-cut, GRIN/ball lens/scattering-sphere terminated, tapered, and side-firing geometries have been employed in the construction of various optical fiber sensors. The different combinations allow for flexibility in desired probing depths and/or collection efficiency of detected light. The relative merits of the selected probe designs will be discussed in subsequent sections of this chapter in the context of a particular modality/application.

17.4 Fiber-Based White Light Spectroscopy

17.4.1 Reflectance Geometry

17.4.1.1 Conventional Reflectance Sensor Design

Light that enters tissue will be scattered and absorbed. The portion of scattered light that escapes the tissue in the backwards hemisphere is termed the diffuse reflectance (e.g., semi-infinite planar geometry, surface irradiation conditions). The diffuse reflectance contains information regarding the scattering and absorption properties of the tissue. The non-invasive nature of surface-probe-based reflectance measurements can furnish a well sampled data set close to and far from the source, yielding

a spatial (and perhaps spectral) reflectance profile well suited for fitting to a theoretical model. As summarized in Table 17.1, the measured reflectance data can be employed to retrieve tissue optical properties, chromophore concentrations, and tissue scattering parameters.

As shown in Fig. 17.9, conventional reflectance sensors employ a single excitation source that injects light into the tissue surface, surrounded by several detection fibers (5–10) at varying distances. To extract the tissue optical properties, the measured reflectance must be fit to an analytic equation, which allows for separation of the absorption and scattering properties [7–9]. The diffusion approximation for a homogeneous, semi-infinite slab is often employed as a model for the purposes of data fitting. Since diffusion theory is valid at positions greater than several mean-free paths (mfp) from the source, this implies source-sensor positions between 0.2 and 2 cm for most tissues. A key advantage of reflectance geometry is that only *relative* data is necessary for determining the optical properties.

Two approaches have been devised for fitting reflectance data. The first is to employ a normal-incidence source and fit the spatially resolved reflectance profile. To enable quantitative data fitting, the entire reflectance profile is normalized to the measured signal at a selected source position. Accurate optical property separation and determination requires that at least one detector fiber be positioned close to the source (~ 0.75 –1 mfp). This is because measurements close to the sources are more indicative of the reduced scattering coefficient, while optical attenuation far from the source represents a combination of both scattering and absorption [10], which is embedded in the effective attenuation coefficient, μ_{eff} .

An alternative configuration, suggested by Wang et al. [9], is to employ an oblique incident source. Here the relative shift in the center of diffuse reflectance from the entry point is employed as additional information to extract the tissue optical properties.

The detection fibers can be packaged in a linear [9] (Fig. 17.9a) or in a circular (Fig. 17.9b) arrangement [10]. The advantage of the circular geometry is that a single source, centered with respect to the detection fibers, can be employed for convenient calibration. The large range of source-detector separations results in a range of reflectance measurements that can span \sim four orders of signal magnitude, complicating simultaneous reflectance measurements at all detector positions. To reduce the dynamic range requirements, neutral density filters are often utilized to attenuate the signals at the closer sensor distances [10]. An alternative approach, suggested by Fuchs et al. [11], is to employ variable integration times (hundreds of milliseconds to a few seconds range) combined with an increased number of detection fibers at larger source-sensor separations, to enhance the detection of low signals.

17.4.2 Depth Sensitivity

Depth-sensitive detection is important for fiber-optic assessment of layered structures. Specific clinical applications include evaluating the dyplastic state of a

particular tissue layer or determining the local uptake of light-activated drugs. Depending on the specific application, a reflectance sensor can be designed to preferentially probe the superficial layer (e.g., 200–400 μm below tissue surface) or furnish information about deeper tissue layers (e.g., 1–2 cm below the surface).

In Section 17.4.1.1, we described the conventional design for typical reflectance sensors. These sensors are not optimized for depth localization. In the following, we focus on design approaches that can be employed to refine the depth selectivity of a reflectance sensor.

In general, two approaches can be employed to separate single or superficially scattered photons from bulk photons that undergo multiple scattering events. The first approach is to maintain the conventional reflectance sensor geometry but employ polarization, time-domain, or frequency domain *gating* techniques by appropriate selection of source and detector characteristics. In this case, multi-layer light modeling may also be required to properly extract the appropriate depth information. The second approach is to adjust the *geometric* attributes of the source and detection fibers employed in the sensor. Here, geometrical parameters of interest are the source-detector (S-D) separation, fiber numerical aperture, fiber diameter, and probe-tissue spacing.

The principles behind these approaches, as well as specific selected examples from the literature, are provided in the following sections.

17.4.2.1 Steady-State Spectroscopy: Geometric Approaches

Source-Detector Spacing

Patterson et al. [12] were able to obtain the average depth from which reflectance information is acquired. From diffusion theory, the steady-state, semi-infinite geometry solution for the fluence rate at a point $P(\kappa, z)$ in a turbid medium (e.g., tissue) is given by:

$$\phi(\kappa, z) = \frac{1}{4\pi D} \left(\frac{\exp \left\{ -\mu_{\text{eff}} \left[(z - z_o)^2 + \kappa^2 \right]^{1/2} \right\}}{\left[(z - z_o)^2 + \kappa^2 \right]^{1/2}} - \frac{\exp \left\{ -\mu_{\text{eff}} \left[(z - z_p)^2 + \kappa^2 \right]^{1/2} \right\}}{\left[(z - z_p)^2 + \kappa^2 \right]^{1/2}} \right) \quad (17.15)$$

where κ is a radial distance coordinate, z is a depth coordinate (i.e. below the tissue surface), $D = 1/3 (\mu_a + \mu'_s)$ is the diffusion coefficient, $\mu_{\text{eff}} = \sqrt{\frac{\mu_a}{D}}$ is the effective attenuation coefficient, $z_o = (\mu'_s)^{-1}$ is the distance of initial scatter from an isotropic point source, $z_e = (5.91)D$ is derived from the extrapolated boundary condition and $z_p = -z_o - 2z_e$ is the location of a negative image source required to meet a zero-fluence-rate boundary condition [12]. Physically, the extrapolated boundary condition assumes that the fluence goes to zero at a certain distance above the tissue surface [13].

The probability that a photon would be re-emitted from the tissue slab and detected by the fiber sensor at location, r , located at the surface, can then be

described by an escape function, E , which is equivalent to the photon current across the boundary at $z = 0$, is given by Fick's Law as:

$$\left(-D \frac{d}{dz} \phi\right)_{z=0} \quad (17.16)$$

Combining Eqs. (17.15) into (17.16) gives the escape function $E(\kappa, \theta, z, r)$:

$$E(\kappa, \theta, z, r) = \frac{1}{4\pi} \left[\frac{z \exp(-\mu_{\text{eff}} k)}{k^2} \left(\mu_{\text{eff}} + \frac{1}{k} \right) - \frac{z_p \exp(\mu_{\text{eff}} l)}{l^2} \left(\mu_{\text{eff}} + \frac{1}{l} \right) \right] \quad (17.17)$$

where k and l are the positive roots of:

$$k^2 = (r - \kappa \cos \theta)^2 + \kappa^2 \sin^2 \theta + z^2 \quad (17.18a)$$

$$l^2 = (r - \kappa \cos \theta)^2 + \kappa^2 \sin^2 \theta + z_p^2 \quad (17.18b)$$

Using Eqs. (17.15) and (17.17), the change in reflectance, $\Delta R(r)$, due to a small absorbing perturbation, $\Delta \mu_a$ in a small incremental volume, dV , is then:

$$\Delta R(r) = \Delta \mu_a \phi(r') dV E(r', r) \quad (17.19)$$

The mean photon-visit depth, $\langle z \rangle_r$, for a source-detector separation of r is then given by:

$$\langle z \rangle_r = \frac{\int_V \phi(r') E(r', r) z dV}{\int_V \phi(r') dV E(r', r) dV} \quad (17.20)$$

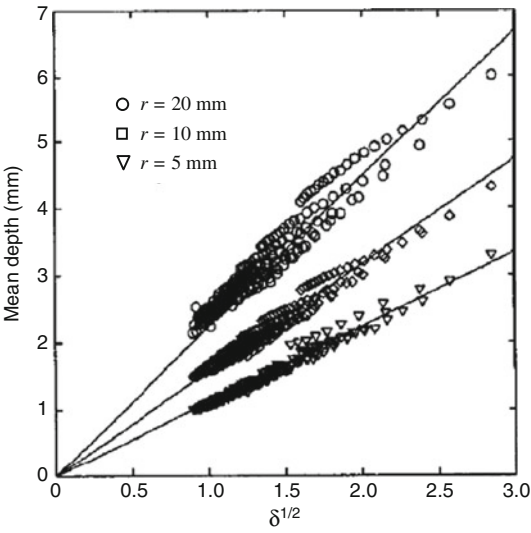
Using Eq. (17.20), Patterson et al. [12] examined the change in $\langle z \rangle_r$ as a function of $\delta^{1/2} = \sqrt{1/\mu_{\text{eff}}}$ (Fig. 17.10). They demonstrated that, using a simple empirical relationship, a reasonable estimation of $\langle z \rangle_r$ could be determined from knowledge of r and δ , alone:

$$\langle z \rangle_r = \frac{(r\delta)^{1/2}}{2} \quad (17.21)$$

From Fig. 17.10 it is clear that short source-detector separations (lower line) result in shorter penetration depths while long source-detector separations (upper line) result in deeper sampling volumes. Furthermore, the mean penetration depth increases with decreasing optical attenuation.

Multi-distance reflectance probes that rely on diffusion theory for data fitting typically involved source-detector separations of up to ~ 2 cm. Such a large probe size may pose serious problems when the optical properties vary significantly over the probe sampling volume (e.g., when evaluating layered structures such as epithelial tissue, or sampling heterogeneous tumors with small localized regions of hypoxia).

Fig. 17.10 Plot of $\langle z \rangle_r$, the mean photon visit depth vs. $\delta^{1/2}$, the square root of the penetration depth. The symbols represent experimental measurements. The lines are a linear fit of the resulting data for each source-detector separation, demonstrating an empirical relationship of $\langle z \rangle_r = \frac{(r\delta)^{1/2}}{2}$ as per Eq. (17.21). (Reprinted with permission from [12])



As demonstrated in Section 17.4.2.1, sensors with shorter source-detector separations (2–3 mm) must be employed to confine the volume of interrogation. An example of one such sensor (employed by Finlay and Foster [14]) is shown in Fig. 17.11 and was used to reveal significant heterogeneities in oxygen saturation in small murine tumor models. However, in these cases diffusion theory is no longer valid. As such, when short-detector spacing is required, alternative forward models and inversion algorithms must be employed during fitting for accurate recovery of optical properties and their spectral dependencies. A brief summary of the different modeling approaches employed for short s–d distances is presented in Table 17.2.

While an exhaustive explanation of all models is beyond the scope of this chapter, in general, the approaches can be divided into improved analytical solutions of the radiative transport equation such as the δ -P1 approximation, Born approximation and P3 approximations, or fast inversion algorithms based on Monte Carlo generated

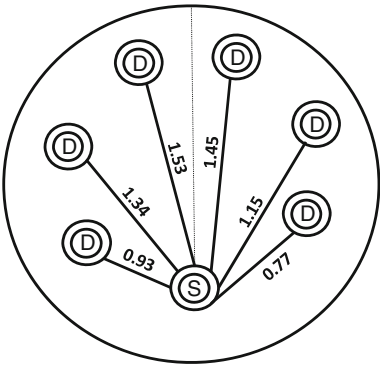


Fig. 17.11 Schematic of a small SD separation reflectance sensor. The source (S) and detector (D) separation distances (mm) are indicated in the figure (after Finlay and Foster[14])

Table 17.2 Analyzing reflectance sensor symbols: models employed for short source detector distances

Model	Application	References
P3 approximation to RTE	Homogeneous medium	Finlay and Foster [14]
δ -P1 approximation to RTE	Homogeneous medium	Seo et al. [15]
Scaled MC	Homogeneous or layered medium	Kienle and Patterson [16]
Born approximation to RTE	Layered medium	Kim et al. [17]
MC-based neural networks	Homogeneous medium	Pfefer et al. [18]
MC-diffusion hybrid	Homogeneous medium	Alexandrakis et al. [19]
Perturbation MC	Layered media	Seo et al. [20]

MC Monte Carlo, *RTE* Radiative Transfer Equation

data (Table 17.2). While analytical solutions carry the advantage of rapid forward calculations, they lack the accuracy of Monte Carlo simulations for many realistic scenarios and geometries. In contrast, Monte Carlo-based strategies are typically accurate but often require longer computational/inversion times.

Specialized Fiber Optic Sensor Geometries

Another approach to superficial depth localization is to employ source-detector separations and geometries that are virtually independent of scattering parameters, such that the path-length is nearly constant across all wavelengths. This is in contrast to the model based approach because it effectively removes the requirement for diffuse light modeling. In these cases, the attenuation effectively reduces to the Beer-Lambert Law, with the change in the measured signal being dictated by the absorption coefficient at each wavelength.

Mourant et al. [21] were the first to demonstrate experimentally that an optimum S-D separation of approximately 1.75 mm resulted in reflectance measurements that were virtually independent of the scattering properties of the measured phantom. These findings were later verified theoretically using diffusion theory [22].

Amelink and Sterenborg [23] developed an approach termed differential-pathlength spectroscopy (DPS) for measuring the optical properties of superficial layers of tissue. The method employs a specialized measurement geometry to reject diffuse light such that the measured signal is relatively insensitive to the surrounding optical properties.

A dual-use delivery-collection fiber (dc) positioned at the tissue surface is used to both illuminate and collect reflected light. A second collection fiber (c) is positioned adjacent to the dc fiber. The c-fiber only detects light that is reflected from the tissue sample. The two fibers are positioned touching side-by-side such that their core-to-core distance is $1.2d_{\text{fiber}}$ where the 1.2 accounts for the presence of the fiber cladding and core. Light collected from the dc fiber contains a combination of both singly backscattered light from *small sample depths* and multiply-scattered, diffuse light from deeper depths.

The principle behind DPS is that when the mean-free-path of photons is much larger than the diameters of the dc- and c- fibers, the probability of collecting *multi-*ply scattered light from deeper depths is roughly equal for both fibers. Furthermore, the probability of collecting *single* scattered from *deeper* depths is also similar. Subtraction of the collection fiber signal, J , from the delivery-collection fiber signal, I , yields a differential measurement, R , that is representative of single-scattered light that predominates from shallow depths.

In this case, the backscattered signal, R^{single} , is approximated by:

$$R^{\text{single}} = C_{\text{app}} \frac{1}{4\pi} \int_{\Omega/NA} d\Omega p(\Omega) Q_{\text{sca}} \rho A \quad (17.22)$$

where C_{app} is a constant that depends on apparatus design and is a function of probe tip, reference material and other components, $p(\Omega)$ is the phase function of the scattering medium, Q_{sca} is the scattering efficiency, ρ is the scatterer concentration (number/volume), and A is the scattering particle area.

For fibers with small numerical aperture (i.e., ~ 0.22), $p(\Omega) = p(180)$ and Eq. (17.22) simplifies to:

$$R^{\text{single}} \approx C_{\text{app}} \frac{1}{4\pi} \int_0^{2\pi} d\phi \int_{\pi-NA}^{\pi} d\theta \sin(\theta) p(180) Q_{\text{sca}} \mu_s \quad (17.23)$$

$$R^{\text{single}} = C_{\text{app}} p(180) \mu_s \quad (17.24)$$

where the scattering coefficient is $\mu_s = Q_{\text{sca}} \rho A$.

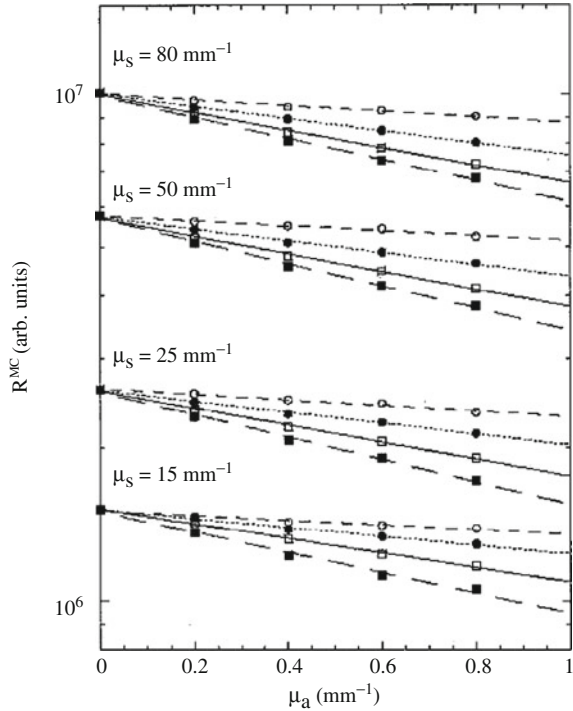
Equations (17.23) and (17.24) have been well described in the literature [24]. However, for most biological tissues scattering is significant and the mfp is typically much smaller than the fiber diameter. In this case, a relatively large number of multiple-scattering events occur at shallow depths close to the fiber tip, and a simple analytical expression is not easily derived. To examine the scattering effects in this regime, Amelink et al. [23] replicated the differential signal, R , using Monte Carlo simulations for a wide range of optical properties ($\mu_s = 15, 25, 50, 80 \text{ mm}^{-1}$, $\mu_a = 0, 0.2, 0.4, 0.6, 0.8 \text{ mm}^{-1}$, $g = 0.9$) typical of biological tissues between 450 and 1000 nm for a range of fiber diameters ($d_{\text{fiber}} = 200, 400, 600, 800 \text{ }\mu\text{m}$).

As shown in Fig. 17.12 (for an anisotropy factor of 0.9 and in the absence of absorption) the differential signal R is almost linearly proportional to the reduced scattering coefficient, $\mu'_s = (1 - g) \mu_s$, such that $R \approx C_1 \mu'_s$ where C_1 is a proportionality constant. Furthermore, the authors demonstrated a Beer-Lambert dependence of the differential signal, R , on the absorption coefficient, μ_a , with a differential path length approximated by $\tau = C_2 d_{\text{fiber}}$. Here, C_2 is a proportionality constant that is ~ 0.95 for most fiber diameters and optical properties. Provided that $\mu_a d_{\text{fiber}} < 0.6$, this value can be used to approximate the differential signal to better than 15%.

Based on the results from the MC simulations the differential signal can be formally summarized as:

$$R = C_1 \mu'_s \exp(-0.95 d_{\text{fiber}} \mu_a) \quad (17.25)$$

Fig. 17.12 Monte Carlo simulation showing Beer's Law behavior, with an apparent path-length being dependant only on fiber diameter: $d_{\text{fiber}} = 200 \mu\text{m}$ (open circles, dashed curves), $d_{\text{fiber}} = 400 \mu\text{m}$ (filled circles, dotted curves), $d_{\text{fiber}} = 600 \mu\text{m}$ (open squares, solid curves), $d_{\text{fiber}} = 800 \mu\text{m}$ (filled squares, dashed-dotted curves). (Reprinted with permission from [23])



Using Eq. (17.25), the optical properties can be extracted using a non-linear multi-parameter fit. However, when the fiber diameter is smaller than the mean free path, single scattering dominates the detected signal. In this regime, the apparent “differential” path-length can be adjusted by changing the fiber diameter. As such, by varying the fiber diameter of the probe, d_{fiber} , the volume of interrogation can be adjusted for the application of interest.

The technique can, therefore, provide highly localized information regarding the absorption and scattering properties of superficial structures with very minimal adjustments in equipment or design. Differential path-length spectroscopy has been employed to perform optical assessment of human breast tissue [25] and oral mucosa [26] as well as localized drug concentrations during PDT [27].

Illumination-Collection Orientation

A possible method to improve depth discrimination of plane-cut fiber reflectance probes is by tilting the orientation of the source or detector fibers at oblique angles to the tissue surface.

Using Monte Carlo simulations, Wang et al. [28] investigated the change in depth sensitivity for reflectance sensors when detection fibers with oblique orientation were employed. In their study, the sensor geometry utilized a single orthogonal

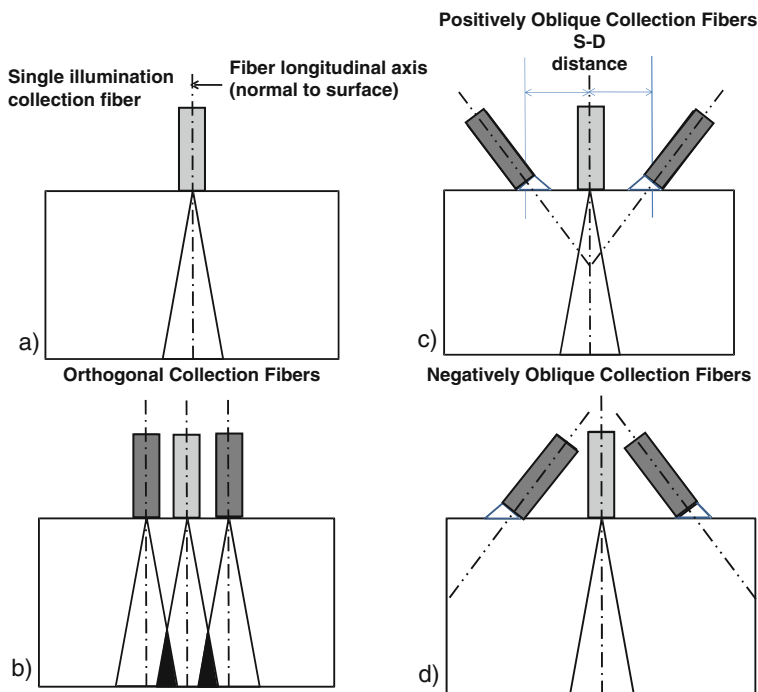


Fig. 17.13 Schematic of the fiber geometries employed for analyzing the effects of collection fiber orientation angle on average depth of penetration of detected photons in reflectance geometry. Grey boxes represent optional index-matching spacers (after Wang et al. [28])

source fiber with detection fibers having varying orientation relative to the surface. The simulated tissue environment mimicked optical properties and geometries representative of human cervical tissues with a thin $450\ \mu\text{m}$ epithelial layer and underlying $10\ \text{cm}$ of stromal tissue.

Figure 17.13 shows the various geometries employed in their study: (a) a single orthogonally oriented illumination-collection fiber; (b) conventional orthogonal fiber geometry; (c) positively oblique detection fibers; and (d) negatively oblique detection fiber geometry. An index matching spacer can be used for tilted fibers to minimize reflections at the air tissue interface and improve detection efficiency. Their results demonstrated that, compared to a perpendicular orientation, positive tilting of the detection fibers results in overlapping illumination-collection volume that is shifted closer to the tissue surface.

Using a zero degree (normal incidence) single fiber geometry as reference (Fig. 17.13a), the authors observed that the mean penetration depth decreases (becomes more shallow) and photon spatial distribution becomes more localized (i.e. better defined) as the collection angle becomes more positive. Since the photons exit the tissue obliquely, they require fewer scattering events and smaller scattering angles before escaping to be detected. Furthermore, the slanted orientation of

the detector improves selection of photons diffusely reflected at small exit angles. The result is that one can obtain improved depth selectivity, and greater sensitivity to optical properties of shallower tissue regions [29–31]. Conversely, increasing the collection angle in the negative direction preferentially selects photons that have traversed deeper tissue regions, while also decreasing the overall peak to width ratio.

The primary limitation of this sensor-tilting approach is that, to maintain small probe dimensions and to prevent mechanical damage, the fibers are generally limited to a maximum tilt angle of $\sim 30^\circ$. For superficial layer sensing, however (Fig. 17.13(c)), this upper threshold still results in a sizeable contribution from photons that have sampled the deeper stromal regions.

A potential solution for obtaining a suitable slanted orientation, proposed by the group at the University of Texas, is to focus the incident beams using a half-ball lens. This approach has been described by Schwarz et al. [32].

Figure 17.14a shows the geometry for a ball lens probe. The total angular deviation of the incident ray, θ , is the cumulative results of refraction at the entrance and exit interfaces of the ball lens.

By geometry (Fig. 17.14b), the angle of incidence, θ_i , can be geometrically related to the distance from the centerline of the ball lens, d , and the ball lens radius and index of refraction, by:

$$\sin \theta_i = \frac{d}{R} \quad (17.26a)$$

$$\theta_i = \sin^{-1} \frac{d}{R} \quad (17.26b)$$

From Snell's law, the refracted angle, θ_2 , at the entrance interface is then related to the index of refraction of air, n_{air} , and the balls lens, n_L :

$$n_{\text{air}} \frac{d}{R} = n_L \sin \theta_2 \quad (17.27)$$

Since $n_{\text{air}} = 1$, the refraction angle is then:

$$\theta_2 = \sin^{-1} \frac{d}{R n_L} \quad (17.28)$$

Performing a similar calculation for the exit angle of refraction, the total angular deviation of the incident ray, θ , is expressed as:

$$\theta = \sin^{-1} \left(\frac{d}{R} \right) - 2 \sin^{-1} \left(\frac{d}{R n_L} \right) + \sin^{-1} \left(\frac{d}{R n_T} \right) \quad (17.29)$$

where n_T is the tissue refractive index.

Using the lens, the incident and collected rays are refracted at oblique angles resulting in a similar distribution that can be obtained by physically tilting the fibers. As the fiber separation increases, the region of intersecting cones moves to

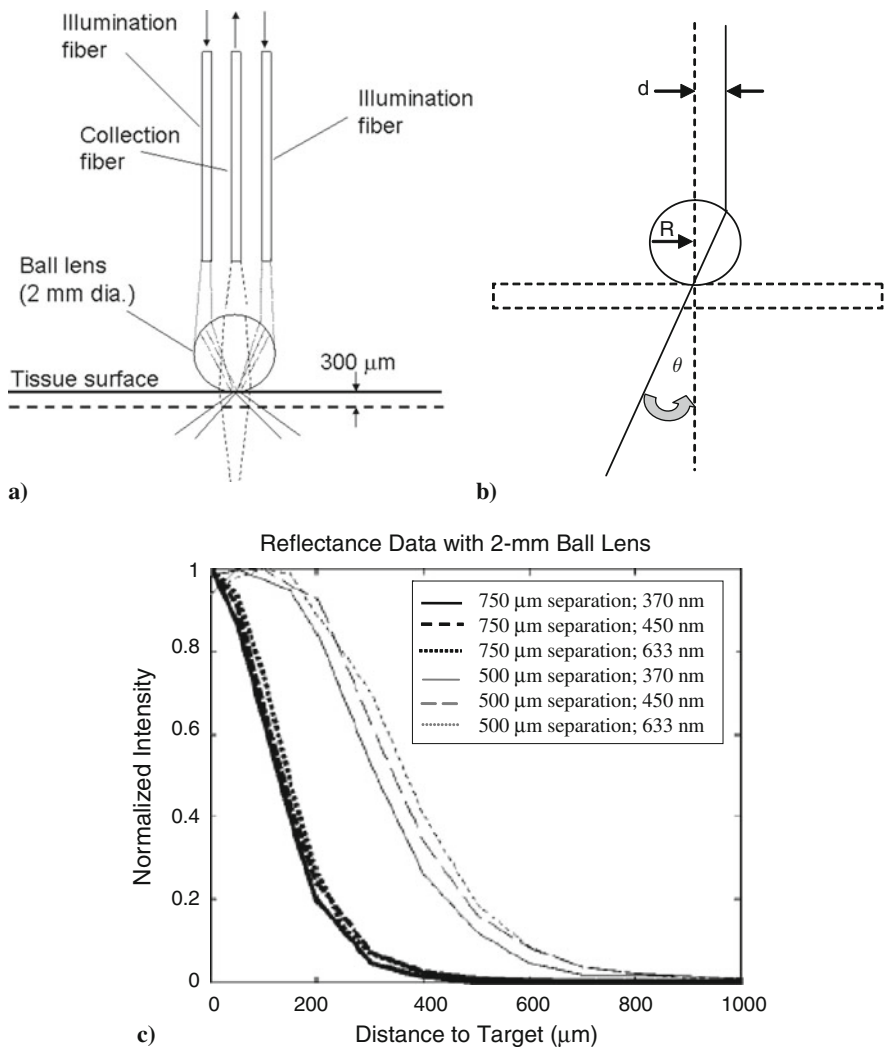


Fig. 17.14 (a) Ball lens sensor composed of a central collection fiber and two adjacent illumination fibers. The separation distance of the illumination and collection can be used to adjust the probing depth of the ball lens sensor: illumination light rays (*solid lines*), detected light rays (*dotted lines*). As reference, the expected thickness of the epithelium ($\sim 300\ \mu\text{m}$) is shown. (b) Geometry for Eq. (17.26). (c) Measured reflectance intensity for a thin scattering layer as a function of ball lens sensor to reflecting target separation, for two different ball lens sensor illumination-collection fiber separations. Note that the depth sensing capability of the sensor is demonstrated by the markedly different reflectance profiles at different illumination-collection fiber separations. (Reprinted with permission from [32])

increasingly superficial depths thereby allowing for preferential selection of shallow penetrating photons (Fig. 17.13b).

Figure 17.13c demonstrates the effects of the ball lens measured experimentally using the geometry of Fig. 17.13a. In these experiments, a thin reflectance target (white business paper) was positioned at different distances from the ball lens sensor, and the reflectance intensity measured as a function of sensor-to-target distance. Two different illumination-collection fiber separations were employed (500 and 750 μm). As expected, the normalized intensity drops faster at shallower depths, as the illumination-collection fiber separation increases.

As noted above, the penetration depth not only depends on physical geometry but on the optical properties of the tissue; an estimate can be obtained via Monte Carlo simulations [29]. In addition to the half-ball lens, a sapphire window can be positioned between the lens and tissue surface to further converge the collection-illumination cones closer to the tissue surface. Arifler et al. [29] have demonstrated that a half-ball lens probe with source-detector fiber separation of 900 and a 300 μm thick sapphire window can result in >98% of collected photons coming from the 300-micron thick epithelial layer (at wavelengths between 450 and 650 nm). The ball-lens sensor has been employed clinically for the diagnosis of cancer of the oral mucosa [33].

Numerical Aperture

The effect of numerical aperture on probing depth is complex and depends on the collection angle of the detection fibers. Using Monte Carlo simulations, Wang et al. [28] have demonstrated that, for collection angles between 0 and 20°, an increase in numerical aperture causes a shift to shallower probing depths. The opposite effect is observed for collection angles between 40 and 75°, whereby the expected probing depth increases with greater NA. In addition to depth selectivity, NA also plays role in signal to noise. For example, increasing the numerical aperture from 0.22 to 0.34 does not significantly change the probing depth of a reflectance sensor but increases the magnitude of the detected reflectance almost two-fold.

17.4.2.2 Polarization Reflectance Gating: Steady-State Spectroscopy

An alternative to mechanical modification of the source and detector fiber orientation is to employ reflected polarized light to preferentially select the detection depth (optical modification) [34]. Polarized light is quickly depolarized upon multiple scattering. As such, reflected photons that are able to preserve their incident linear polarization are typically representative of light scattering in *upper layer* tissues. In contrast, detection in a *crossed-linear* sensor picks up mostly depolarized light randomized by multiple scattering, indicative of *deeper tissue layers* (and/or any circularly polarized light that may be present). Hence, the crossed polarized reflectance can be subtracted from the parallel component to isolate reflectance originating from superficial depths. The resulting polarization measurement $D(\lambda)$ is given by:

$$D(\lambda) = \frac{I_{\parallel}(\lambda) - I_{\perp}(\lambda)}{I_{\parallel}^S(\lambda) + I_{\perp}^S(\lambda)} \quad (17.30)$$

Here $I_{\parallel}(\lambda)$ is the parallel polarized light relative to the incident light, $I_{\perp}(\lambda)$ is the perpendicular polarized light relative to the incident light, and λ is the wavelength of the incident light. The denominator is employed for normalization and is the sum of the perpendicular, $I_{\perp}^S(\lambda)$, and parallel, $I_{\parallel}^S(\lambda)$, components collected from a diffusing calibration medium. By normalizing, the detected signal now accounts for systematic sensor parameters such as the source and spectrometer spectral characteristics.

A simplified fiber polarization reflectance probe utilized by Johnson and Mourant [34] is shown in Fig. 17.15.

The probe is composed of a source (a) and two detection fibers for collection of parallel and cross polarized light. The source and one detection fiber are covered with a linear polarizing film while a different cross polarizing film covers the other detector. Myakov et al. [35] employed a similar sensor configuration to measure the reflectance spectra of oral cavity mucosa in vivo. The resulting spectra can be fit using Mie theory to obtain estimates of nuclear size for cancer detection. In this case, the polarization ratio is related to the average nuclear diameter, \bar{d} , and the number of nuclei per unit volume, ρ , by:

$$D(\lambda) = \frac{I_{\parallel}(\lambda) - I_{\perp}(\lambda)}{I_{\parallel}^S(\lambda) + I_{\perp}^S(\lambda)} a(\rho) B(\lambda) + b(\rho) S(\lambda) F(\lambda) + S(\lambda) \quad (17.31)$$

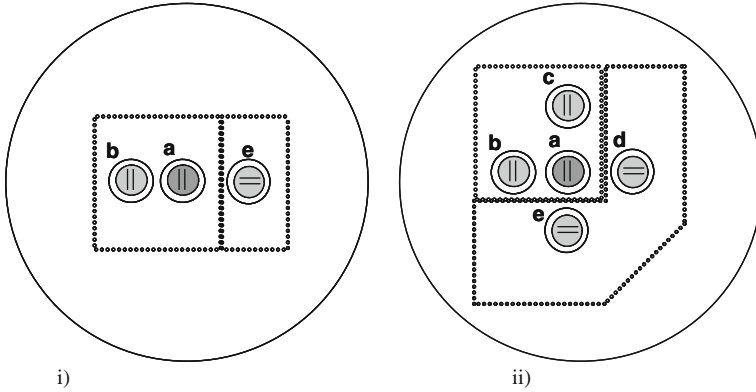


Fig. 17.15 Polarized reflectance sensor: The *dotted lines* within the sensor are representative of polarizing sheets while the *parallel lines* within the circular fibers are representative of the polarization orientation: (i) Polarized reflectance probe (*front view*) composed of an illumination channel (label **a**) with parallel (label **b**) and cross-polarized (label **c**) detection fibers (ii) This probe configuration employs an illumination fiber (label **a**) with two parallel detectors (labels **b** and **c**) and two cross-polarized detectors (labels **d** and **e**) such that all four polarization permutations can be measured (after Johnson and Mourant [34])

with

$$F(\lambda) = \int_{\theta_F} p(\theta, \lambda, \bar{d}, \Delta d) \sin \theta d\theta \quad (17.32)$$

$$B(\lambda) = \int_{\theta_D} p(\theta, \lambda, \bar{d}, \Delta d) \sin \theta d\theta \quad (17.33)$$

$$p(\theta, \lambda, \bar{d}, \Delta d) = \langle p(\theta, \lambda, \bar{d}, \Delta d) \rangle_{N(d)} = \int_0^\infty p(\theta, \lambda, \bar{d}, \Delta d) N(d) dd \quad (17.34)$$

where d is the diameter of the nucleus, $p(\theta, \lambda, \bar{d}, \Delta d)$ is the scattering phase function averaged over a distribution of nuclear diameters, $N(d)$, Δd is the standard deviation of the average nuclear diameter, θ is the angle between the detection and illumination angles, θ_D is the backward scattering angle range, θ_F is the range of scattering angles in the forward direction, $a(\rho)$ and $b(\rho)$ are nuclei density dependent parameters, and $S(\lambda)$ is the depolarization ratio profile of underlying tissue that can be determined experimentally. The term $p(\theta, \lambda, \bar{d}, \Delta d)$ is based on Mie theory – with the assumption that the nuclei are homogeneous spheres – and contains information regarding the nuclear diameter distribution, as well as, the spectral dependence of the scattering coefficient.

Groner et al. [36] employed a similar approach to reduce confounding specular reflection signals and enhance the contribution of light detected from deep tissue layers.

17.4.2.3 Time-Resolved Reflectance Spectroscopy

Diffusion theory can also be used to obtain the average penetration depth, $\langle z \rangle_r$, as a function of detection time for time-resolved fiber optic reflectance sensors [12].

In the time-domain case, we are interested in the fluence rate as a function of time at source-detector separation, r , and time, t , following an impulse source. Here, the decrease in photons that escape the tissue due to an absorption inhomogeneity in dt' at r' is:

$$\Delta R(r, t, t') = \Delta \mu_a \phi(r', t') dV E(r', r, t - t') dt' \quad (17.35)$$

Here, $\phi(r', t')$ and $E(r', r, t - t')$ are the time-resolved equivalents to the continuous wave fluence rate and escape function, respectively. They are given by:

$$\begin{aligned} \phi(\kappa, z, t') &= c(4\pi Dc)^{-3/2} t'^{-3/2} \exp(-\mu_a c t') \\ &\times \left\{ \exp \left[\frac{(z - z_o)^2 + \kappa^2}{4Dc t'} \right] - \exp \left[\frac{(z - z_p)^2 + \kappa^2}{4Dc t'} \right] \right\} \end{aligned} \quad (17.36)$$

$$E(\kappa, \theta, r, t - t') = \frac{1}{2} (4\pi Dc)^{-3/2} |t - t'|^{-5/2} \times \exp(-\mu_a c |t - t'|) \\ \times \left\{ z \exp\left[\frac{\kappa^2}{4Dc |t - t'|}\right] - z_p \exp\left[\frac{l^2}{4Dc |t - t'|}\right] \right\} \quad (17.37)$$

where c is the speed of light in tissue.

Integrating overall possible time, t' , gives the total reduction in photons, $R(e, t, t')$ as:

$$R(r, t) = \Delta\mu_a dV \int_{|r'|/c}^{t-|r-r'|/c} \phi(r', t') E(r', r, t - t') dt' \quad (17.38)$$

The mean penetration depth for a source-detector separation of r and time of detection, t , is described by:

$$\langle z \rangle_r = \frac{\int_V z dV \int_{|r'|/c}^{t-|r-r'|/c} \phi(r', t') E(r', r, t - t') dt'}{\int_V dV \int_{|r'|/c}^{t-|r-r'|/c} \phi(r', t') E(r', r, t - t') dt'} \quad (17.39)$$

Equation (17.39) can be evaluated using numerical integration. An example is shown in Fig. 17.16 for a nominal set of optical properties. As expected, it is seen that increasing the detection time results in deeper sampling volumes. As such, the depth of penetration can be adjusted at a single source-detector distance by varying the detection times of a time-domain reflectance sensor.

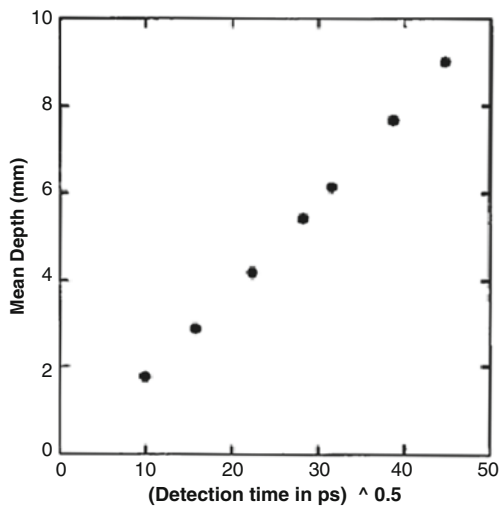


Fig. 17.16 Plot of mean photon visitation depth versus the square root of the detection time using a pulsed source and time-gated detection system. Here $\mu'_s = 10\text{cm}^{-1}$, $\mu_a = 0.1\text{ cm}^{-1}$, $c = 0.214\text{ mm ps}^{-1}$, and the source-detector distance of the surface sensor is 10 mm. (Reprinted with permission from [12])

17.4.3 Interstitial Geometry

The advent of optical-based treatments such as photodynamic therapy (PDT) and laser thermal therapy (LTT), often applied interstitially, has increased the necessity for corresponding interstitial sensors that can provide information for pre-treatment planning, and for on-line monitoring of treatment progress. Interstitial sensors measure the internal fluence or radiance (see [Chapter 2](#) of this text for a review of these terms) in a turbid medium to extract information on either the light (directional or integrated) intensity (dosimetry), optical properties (spectroscopy), or extent of treatment effect. The following section reviews the basic design of fluence and radiance probes, followed by clinical applications specific to the interstitial geometry.

17.4.3.1 Fluence Sensors

Spherically Diffusing Tip

Conventional interstitial fluence sensors are constructed by attaching a minimally-absorbing, highly scattering sphere to the end of a plane cut fiber (Fig. 17.17a). Since light entering the diffusing sphere is multiply scattered, the incident light is effectively collected over all polar and azimuthal angles by the plane cut fiber (typically 400–600 μm core diameter) with virtually equal probability over all polar and azimuthal angles. Monte Carlo simulations comparing the fluence with and without a sensor have demonstrated that spherical fluence sensors with diameters as small as 0.5–0.8 mm result in minimal perturbation to the true fluence field in the turbid medium [37].

Two approaches have been reported for constructing the scattering tip. The first employs a UV-curable epoxy polymer mixed with a highly scattering powder (typically titanium dioxide) [38]. A plane cut fiber emitting UV light at microwatt powers

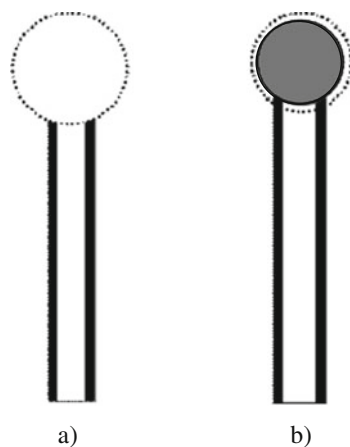


Fig. 17.17 (a) Sphere-tipped fluence probe with scattering sphere attached to the end of a plane cut fiber
(b) Integrating sphere fluence probe with a constructed ball-tipped fiber coated with a thin layer of scattering material

is shone into the epoxy mixture. The resulting fluence pattern is then an isotropic spherical distribution that forms symmetrically around the fiber tip. Following the formation of the scattering tip, the epoxy is irradiated at higher powers to fully solidify.

A variation of this geometry is to employ a fiber with a ball-shaped tip instead of a plane cut fiber and grow a thin layer of scattering material around the tip (Fig. 17.17b). The spherically tipped fiber can be purchased through commercial vendors, or constructed in-house by employing a small torch to melt the fiber tip at temperature $>2500^{\circ}\text{C}$ to the desired ball shape. Here the optical fiber tip acts as an integrating sphere and requires less scattering epoxy compared to a bare-tipped fiber to fully randomize the direction of the incoming light. An additional advantage of this configuration is that if the fluence sensor is employed as an isotropic spherical source, higher input powers can be utilized, since the absorbed heat is dissipated over the entire spherical surface instead of being concentrated in the vicinity of the smaller bare-tip area.

A second method is to attach a pre-fabricated sphere, typically made of Arnite, ceramic, or Teflon, to the end of a bare tip, plane cut fiber [39, 40]. A small hole is bored to the center midway point of the sphere, the sphere is then “skewered” by the fiber and fixed using glue to the end of the fiber tip.

The primary weakness of scattering sphere probes is that sizeable diameters ($\sim 1\text{--}2\text{ mm}$) are required to achieve a desired level of collection isotropy and that an inherent “blind-spot” is present at the stem region of the probe. Typically, a 3 mm-diameter probe can achieve an isotropy to within $\pm 15\%$, while a $\sim 1\text{ mm}$ -diameter probe is isotropic to within $\sim \pm 20\%$ over a 320 angular range [39, 40]. Finally, during clinical application, the spherical tip can become unattached from the fiber core if the sensor is pulled back too quickly or awkwardly during its positioning, manipulation, or removal.

Fluorescent Dye-Loaded Tip

To overcome the size limitations of scattering-sphere probes, Lilge et al. [41] developed fluorescent dye-loaded fluence sensors. The use of fluorescent dyes overcomes the limitations of larger scattering-based spherical sensors, because fluorescence emission is naturally isotropic. As such, the isotropy of the sensor is dependent only on the tip shape and not its size [41].

The sensor designs are illustrated in Fig. 17.18. First, a polymethyl methacrylate (PMMA) dye-free offset is attached to the end of a plane cut fiber (Fig. 17.18a). The offset effectively serves as a spacer between the dye-sensitive region and the fiber. Next, a dye-loaded PMMA tip is added to the offset. The dye-free and dye-loaded PMMA are constructed using methyl-methacrylate (MMA), which is polymerized in an oven at 60°C for $\sim 48\text{ h}$ and initiated using a primer (Azobis, Polyscience, Milwaukee, WI, USA). The addition of dimethyl chloride (DMC) changes the solid polymerized PMMA to a viscous form. As such, fluorescent dyes dissolved in DMC can be added to the solid PMMA. Following evaporation of DMC, the dye remains absorbed in the PMMA.

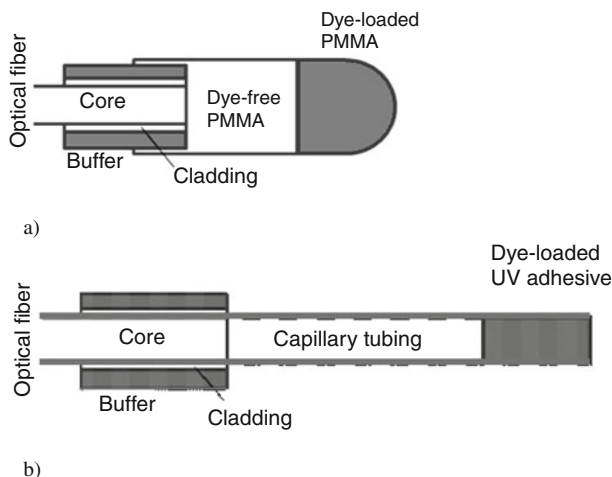


Fig. 17.18 Fluorescent dye-loaded fluence sensors: (a) Dye-loaded PMMA design; (b) Capillary tube tip design with dye-loaded UV adhesive (after Lilge et al. [41])

Fiber tips with total diameters ranging from ~ 250 to $435 \mu\text{m}$ can be constructed using this approach. Smaller tips ($<200 \mu\text{m}$ diameter) can also be produced by attaching a section of dye-filled silica capillary tubing to the end of an optical fiber (Fig. 17.18b). The capillary tube is filled at the end with a dye-filled epoxy, which is cured internally inside the tubing.

The polar isotropy of the sensor is typically $\pm 10\%$ between 0° and 160° for probe tips $<400 \mu\text{m}$, although angular variations as large as $\pm 20\%$ have been noted (caused by difficulties in consistent tip construction). These values are comparable to the response of spherical fluence sensors. The primary disadvantage of dye-doped sensors is their limited lifetime that stems from photodegradation of the fluorescent dye. As such, fluorescent probes should not be considered for long term extended use, especially if employed for dosimetric purposes. Furthermore, the relatively low damage thresholds negates the usage of such probes in some scenarios (e.g., for high-powered ($>400 \text{ J}\cdot\text{cm}^{-2}$) laser thermal therapy monitoring applications).

Calibration

Fluence sensor calibration is required for: (1) light fluence dosimetry (for example during PDT) and (2) absolute optical property determination. The light collected by a fluence sensor is directed to a photodiode or photomultiplier tube and is converted to a photovoltage (V) that is proportional to the true fluence, ϕ , related to each other by:

$$\phi = A(V - B) \quad (17.40)$$

where A is the calibration constant ($\text{mW cm}^{-2} \text{ V}^{-1}$), and B (volts) is a factor that accounts for the leakage of the detector. Typically, fluence sensors are calibrated in air either using a collimated light source [39] or in an integrating sphere [42]. When applied to tissue, additional calibration factors must be employed to correct for the index of refraction differences between air and tissue, fluence perturbation from the scattering tip, the blind spot from the fiber stem, and non-isotropic responses of the scattering bulb [40].

17.4.3.2 Pre-Clinical and Clinical Applications

Non-invasive surface reflectance geometries allow for a well-sampled data set of radially-resolved surface measurements, which allows for the determination of both μ'_t and μ_{eff} , and thus the unique determination of absorption and scattering. However, interstitial characterization is complicated by: (1) the necessity to limit patient invasiveness and (2) limitations in sensor positioning due to insertion through guidance templates. Clearly, the number of physical allowable measurement positions is limited when inserting sensors directly into tissue. As such, a particular challenge of interstitial geometries is to devise strategies for uniquely separating absorption and scattering properties using measurements far from the source, where optical properties cannot be uniquely separated with relative measurements alone.

Calibrated sensors effectively overcome the limitations of poor spatial sampling by measuring differences in intensity at positions far from the source that are dominated by $\mu'_t = \mu_a + \mu'_s$ and not μ_{eff} . However, accurate calibration can be difficult to accomplish and must be performed for each source-detector pair and for different irradiation wavelengths during spectroscopy. Several interstitial techniques have been devised to avoid absolute calibration when determining tissue optical properties at single wavelengths.

Dimofte et al. [42] have employed multiple fluence sensors and sources attached to a scanning translation stage coupled to a common catheter, for optical property determination during PDT of the prostate. The set-up allows for multiple spatial measurements to be acquired in the *same* catheter, thereby avoiding additional insertions. Optical properties can be assessed throughout the prostate volume in quadrants with different source-detector pairs sampling a different volume of the prostate. A similar approach, reported by Pomerleau-Delacourt and Lilge [43], is to employ fluorescent sensors with multiple detection locations along the same fiber.

Interstitial optical measurements have recently been developed for monitoring of thermal damage during laser thermal therapy (LTT) [5]. The approach relies on the significant difference in scattering between native and thermally coagulated tissue. The optical approach carries two significant advantages compared to conventional temperature sensors used for monitoring LTT. First, due to the speed of light in tissues, optical measurements provide volumetric information in near real-time even at positions distant from the source. This is in contrast to temperature sensors, where charring or coagulation events can occur some tens to hundreds of seconds before manifesting as a temperature change at typical monitoring positions of 0.5–1 cm from the source. Second, temperature sensors are unable to directly monitor thermal

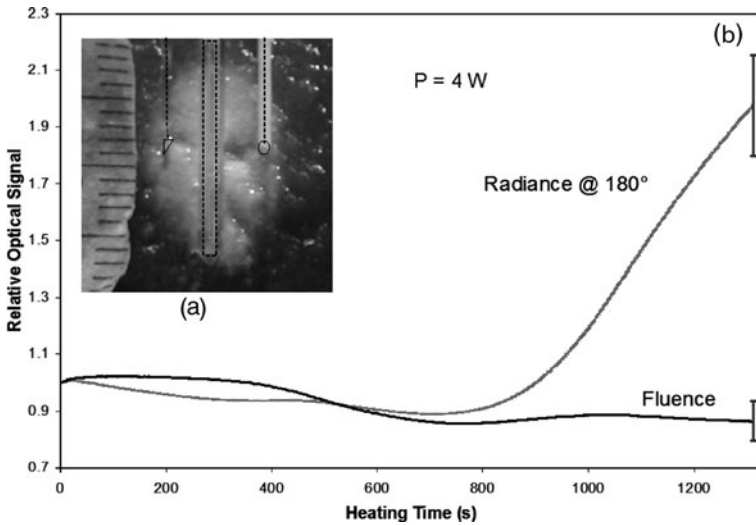


Fig. 17.19 (a) Optical monitoring of coagulation boundary using real-time optical fluence measurements (source power (P), source-detector separation (r)). As the coagulation boundary approaches the fluence sensor, a decrease in light intensity is observed. This is due to a “light trapping” effect from the increased scattering properties of coagulated tissue. The same effect causes an increase in light intensity when the coagulation boundary reaches the location of the fluence sensor (located approximately at the *triangle*). Hence, a fluence sensor can be positioned strategically at the boundaries of a tumour to terminate the LTT treatment. The inset is a photograph of the resulting region of damage following LTT, indicating the locations of the source and detectors employed for optical monitoring. Note that, as expected from the termination of the treatment due to the increase in fluence, the damage boundary is located almost at the location of the fluence sensor (b) Comparison of fluence and 180° radiance measurements for optical monitoring of the coagulation boundary in tissue simulating optical phantoms. The 180° radiance enhances the sensitivity to the passing of the coagulation boundary compared to fluence measurements. (Reprinted with permission from [5])

damage and instead rely on thermal dose models or threshold temperatures to estimate the extent of coagulation. However, optical sensors are able to directly measure coagulation changes that are independent of the thermal dose models.

Figure 17.19a illustrates the concept of optical monitoring during LTT of ex vivo bovine liver. As the coagulation boundary approaches the fluence sensor location, a decrease in light intensity is observed. This is due to a “light trapping” effect from the significant increase in optical scattering within the coagulated region. This same scattering increase results in a significant increase in light intensity when the coagulation boundary reaches the sensor location. Hence, a fluence sensor strategically positioned at the margins of a cancerous region could be used to terminate an LTT treatment and spare healthy surrounding tissue. In addition, directional light measurements (radiance) measurements can be employed instead of (isotropic) fluence sensors to offer enhanced sensitivity to the passing of the coagulation boundary. In particular, Chin et al. [5] demonstrated in tissue simulating phantoms that the backwards (or 180° radiance) provides almost a two-fold increase in sensitivity

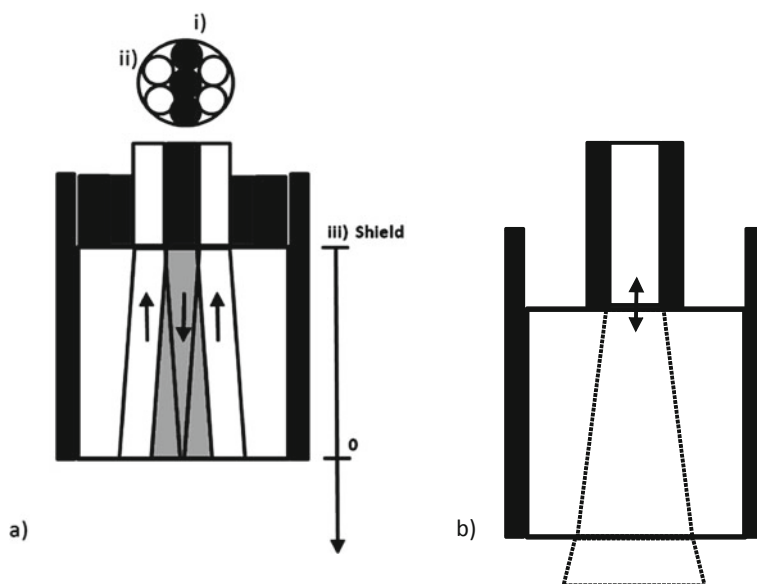


Fig. 17.20 Conventional fluorescent sensors. (a) Multi-fiber design (i) excitation fibers, (ii) collection fibers and (iii) quartz shield (b) Single fiber design: variable aperture (after Utzinger and Richards-Kortum [2])

compared to fluence measurements (Fig. 17.20b). They demonstrated that the light intensity increase from the passing of the coagulation boundary is primarily due to the increase of backwards traveling light randomized by the increased scattering properties of the coagulated region. Hence unlike fluence measurements, 180° radiance sensors effectively “filter out” the radiance that is insensitive to the passing of the coagulation volume.

The optical approach provides virtually instantaneous information regarding the onset, approach and final extent of thermal damage. Combined with interstitial temperature sensors, optical monitoring can be employed as a feedback technique to adjust laser power levels and determine treatment termination when complete coverage of the target volume is achieved. As such, optical monitoring provides the advantages of volumetric information of thermal damage with the simplicity point optical sensor technology.

17.5 Fluorescence Spectroscopy Fibers

17.5.1 Basic Approach

Fluorescence spectroscopy is widely used for the detection and evaluation of neoplastic tissues. The technique is potentially able to provide quantitative information regarding the biochemistry, morphology and composition of pre-cancerous lesions

in several tissues including cervix, esophagus, bronchus, colon and skin. The primary fluorescent tissue components, or fluorophores, are structural proteins such as pyridine nucleotide, collagen, tryptophan, porphyrins, elastin, and flavoprotein [44]. The presence and relative concentration of these fluorophores and their distribution in tissue provides a means of distinguishing between normal and cancerous tissues. In addition, the technique is able to provide dosimetric information and treatment evaluation of photonic treatments such as PDT and LTT. In the case of PDT, fluorescent probes can be employed to determine the localization and concentration of drugs (exogenous photosensitizers) necessary for treatment effect, as well as photobleaching for treatment monitoring.

Given the range of target sites evaluated by fluorescence spectroscopy, it is important to design fiber sensors that provide customized capabilities for their specific clinical applications. In the following section we describe a typical fluorescent sensor and the specific design characteristics that influence the detected signal.

17.5.2 Fluorescence Sensor Design

Similar to elastically-scattered light sensors of section 4, a conventional fluorescent sensor consists of (a) an excitation fiber, (b) a collection fiber and (c) a quartz shield (employed as a spacer). Carbon-filled or low-fluorescent epoxy can be employed to hold the fibers. Two potential configurations exist. In the first, the excitation and collection fibers can be comprised of separate fibers (Fig. 17.20a). Alternatively, a single excitation-collection fiber (Fig. 17.20b) can be employed for a more localized fluorescence measurement. Multi-fiber sensors employ fiber bundles at different detection locations to achieve an overall larger interrogation volume. This configuration is particularly attractive for characterizing larger tissue, or when the margins or location of a suspected lesion are unknown.

17.5.2.1 Single and Multi-Fiber Sensors: Pros and Cons

It is important to compare the relative merits of single fiber and multi-fiber (i.e. multi-distance) fluorescent sensors. Both simulation and phantom experiments have demonstrated that single fiber probes provide improved signal intensity and greater sensitivity to superficial fluorophores. This is primarily due to the overall shorter pathlengths traveled by collected photons in the single-fiber geometry. In contrast, multi-fiber separation probes detect photons that travel longer pathlengths and, as such, are more sensitive to distortions and signal loss from blood absorption. For shorter separations, multi-distance sensors can still provide reasonable depth sensitivity with peak fluorescent detection sensitivity of ~ 0.1 mm depth per 0.1 mm separation, up to 0.4 mm. Beyond ~ 0.4 mm larger separations result in a virtually uniform sensitivity to all depths.

Zhu et al. [45] described a 7-fiber sensor that combines the benefits of both single and multi-distance designs. In their configuration a central fiber is surrounded in a ring by six additional fibers. The central fiber acts as a single fiber (illumination

and collection) sensor providing superficial probing sensitivity. The central fiber and one of the surrounding fibers can also be utilized in parallel for illumination and collection as a larger diameter ‘single fiber’ sensor to provide intermediate depth sensitivity. Finally, the central fiber and one of the surrounding fibers can be employed as a multi-fiber sensor (one fiber illuminating and the other fiber detecting) as a means to provide information on deeper-seated structures.

17.5.2.2 Effect of Spacer-Thickness

The shield/spacer thickness, typically 1–7 mm, determines the fiber(s)-tissue separation and is a vital sensor design parameter. In the absence of a spacer (i.e., zero fiber-tissue separation, contact sensor) the excitation and detection regions are not co-localized. Therefore, light must travel laterally through the interrogated tissue before being collected, thereby increasing the overall path-length and decreasing the intensity of detected photons due to attenuation. However, by increasing the fiber(s)-tissue distance, the spacer allows the excitation and collection regions to intersect, causing a decrease in the average lateral distance required for fluorescence collection, and correspondingly, an increased collection efficiency and improved sensitivity to fluorophores located in superficial regions. Note that, as described in Section 17.4.2.1, by adjusting the source-detector separation, the mean probing depth of detected photons can also be adjusted for steady-state reflectance sensors.

The collection efficiency, β_t , for a multi-fiber sensor (depicted in Fig. 17.20a) has been described by [46]:

$$\beta_t = \frac{\beta_0}{(z + \text{shield}_t)^2} \quad (17.41)$$

where z is the sensor to tissue distance along the optical axis of the sensor, shield_t is the length of the spacer cap, and β_0 is a constant that incorporates the detector efficiency. Equation (17.41) assumes isotropic fluorescence emission and does not hold for tissues with high forward scattering. For example, in arterial tissue, the collection efficiency has been shown empirically to follow a $1/\text{shield}^n$ dependence, with $n \sim 1.1$ [47].

Equation (17.42) breaks down for very small spacer thicknesses < 0.5 mm [48]. This is due to a shift in the overlap of the excitation and collection volumes of the sensor. When no spacer is employed, the collection fibers do not directly view the region of excitation. Here, photons must travel laterally (hence, be attenuated) before being detected. However, as the spacer size increases slightly, the overall field of view of the collection fibers increases such that the collection fibers directly view the excitation spot. In this case, no lateral propagation is needed for detection and the sensor preferentially detects superficial fluorescence. In this spatial window, an increase in β_t is observed. Beyond this regime, the increasing overlap of the excitation-collection volumes now detects a greater proportion of deeper lateral-traveling photons with longer path-lengths, thereby decreasing the collection

efficiency. Equation (17.42) is representative of this latter regime. Single-fiber sensors, which obviously have the greatest volume of illumination-collection overlap also exhibit such trends.

It is important to note that the larger the shield thickness, the larger the diameter of the shield and, consequently, the overall sensor diameter. To reduce the overall diameter, the quartz spacer may be substituted using a coated glass rod or thick portion of optical fiber. These elements can effectively mix the illumination and collection volumes of the sensor. With this design, illumination and collection fibers are stripped of their outer jacket, randomly fixed with epoxy and packed hexagonally into a thin glass rod held together using shrink tubing. This greatly reduces the overall diameter of the resulting sensor, while maintaining the high collection efficiency of larger diameter spacer-based sensors. To ensure uniform illumination, the length of the rod should be greater than $2R_{\text{fiber}}/NA$, where R_{fiber} is the radius of the illumination and collection fibers.

17.5.2.3 Fiber Diameter and Orientation

Similar to reflectance spectroscopy sensors (Section 17.4.2.1), varying both the source and collection diameter has shown to influence the depth sensitivity of collected fluorescence. Monte Carlo models and phantom studies have been performed to elucidate the influence of sensor design on both the intensity and primary origin of the detected fluorescence signals [45, 48].

For small diameter fibers, sensitivity to superficial depths can be observed. This is a result of the reduced number of possible path-lengths of fluorescence photons for detection. However, with larger diameters the fluorescence sensitivity is averaged over many depths, thereby homogenizing and increasing the overall signal. These changes are due to the same physical effects that occur with varying source-detector separation: an increase in measured photons that travel longer and deeper paths through tissue before being collected.

Previous studies have demonstrated that, in the range of 0.22–0.4, increasing the collection fiber numerical aperture results in an increase in collected intensity and an enhancement in fluorescence sensitivity to superficial layers. These trends are thought to stem from the increased acceptance angle afforded by larger NAs that allow for the collection of higher angle photons that originate under the illumination region. However, beyond an NA of 0.4, the collection efficiency ceases to increase significantly due to the longer path-lengths of high angle photons, resulting in significant photon attenuation [48].

Orienting the excitation fiber to greater than 45° incidence has shown to enhance collection efficiency and increase sensitivity to superficial layers [45]. This is because angled illumination results in a shallower excitation light distribution, which leads to a shallower volume of origin for the generated fluorescence. Recall that a similar principle can be employed for depth discrimination for spectroscopic reflectance sensors (Section “Specialized Fiber Optic Sensor Geometries”). However, for illumination angles less than $\sim 30^\circ$, very little difference in detected fluorescence characteristics is observed compared to normal illumination.

17.5.2.4 Effect of Illumination-Collection Fiber Separation

Compared to single-fiber sensor, multi-fiber sensors also offer the additional flexibility of varying the illumination-collection fiber separation. This provides an additional parameter for depth selectivity [48]. In general, increasing the illumination-collection spacing results in the detection of fluorescent photons from deeper regions. Again, physically this is explained by the longer path-lengths required for collection when larger fiber separations are employed.

17.5.3 Influence of Tissue Optics

While sensor design parameters influence the depth of fluorescence origin and average path length of detected photons, the detected fluorescent intensity and measured spectrum is also “distorted” by optical properties of the interrogated medium. A number of investigators have examined the effect of absorption and scattering on the “intrinsic” fluorescence spectrum [48–50]. These studies have shown that spectral alterations due to optical properties tend to be enhanced when detected photons travel longer path lengths within the tissue. Hence, probe designs with large diameters, large NA, shallow illumination angle (i.e., near normal incidence), small source-tissue spacing, and large source-detector spacing will suffer greater changes than their opposite counterparts.

While sensor design can be utilized to minimize the effects of tissue optical properties, an alternative approach is to correct the altered spectra through reflectance data that provide an indication of the degree of fluorescent distortion by combining reflectance-and fluorescence spectroscopy. The most straightforward approach is to utilize the measured reflectance to quantitatively derive information regarding the tissue optical properties (penetration depth, absorption and scattering). Using the measured optical properties, the “intrinsic” fluorescence spectra can be corrected using appropriate photon migration models. While early corrections required simplified geometries such plane-wave irradiation and/or specific source-detector arrangements [51–53], recent improvements in diffuse light models have extended the technique to more complicated three-dimensional geometries [55, 56].

A more simplified approach is to employ an approximate relationship between the measured fluorescence and reflectance to correct for spectral distortions. Finlay et al. [54] recently described an empirical correction method by dividing the measured fluorescence spectrum by the reflectance signal measured at the same wavelengths. The approach, which does not require determination of tissue optical properties, is applicable over a wide range of reflectance measurements typically encountered in vivo. However, their correction is limited to fixed source-detector geometries.

Another alternative is to employ the distorted fluorescence spectrum to directly obtain information regarding the sample’s optical properties, and then employ the determined optical properties to eliminate the distortion. Using a forward-adjoint model, Finlay and Foster [56] have demonstrated that it is, in fact, possible to

directly recover the intrinsic fluorescence and information on tissue optical properties from the measured distorted spectrum. Future advancement of this concept will likely allow for fluorescent corrections without the necessity of added reflectance components, thereby greatly simplifying detection technology and computational analysis.

17.6 Optical Coherence Tomography Fibers

Unlike other fiber sensors described in this chapter, OCT forms truly depth-resolved tomographic cross-sectional images, with a depth resolution in the 1–20 μm range (cf. “depth-sensing” discussions of various sensors above). Essentially, an OCT imaging sensor forms the sample arm of an OCT interferometer and typically consists of a single mode optical fiber terminated with a focusing element (e.g., a GRIN or a ball lens) and beam deflecting element (e.g., a retro-reflecting prism or an angle cleaved distal optic) for a side-viewing sensor. The overall principle can be appreciated from the layout of a catheter-based fast OCT imaging system presented by Tearney et al. [57], as shown in Fig. 17.21. Specifics of the distal sensor design, combination of radial scanning and longitudinal fiber pull-back approach, and integration with the rest of the OCT imager can be enabled. Using the system in Fig. 17.21 and its later variants, the authors were able to generate impressive subsurface images of the superficial layers of the gastro-intestinal and broncho-pulmonary tracts, as well as intravascular images of atherosclerotic plaques in coronary arteries [58]. Several other groups have also developed their own versions of intravascular and endoscopic OCT imaging systems, all using their own unique implementations of OCT fiber sensors. For example, Fig. 17.22 shows an endoscopic sensor developed by Yang et al. [59] for esophageal imaging in the gastrointestinal tract.

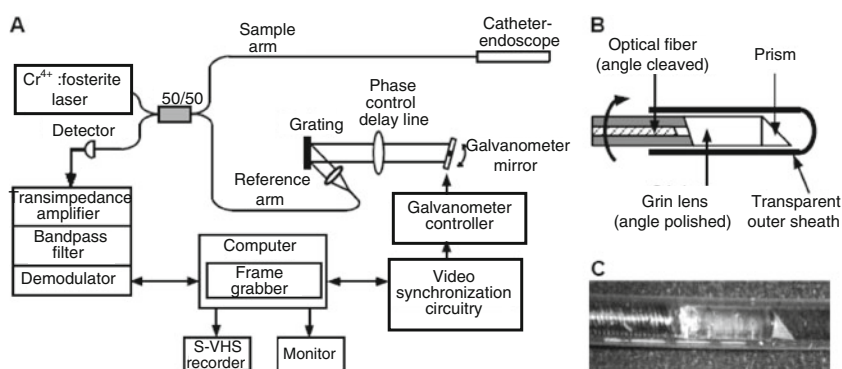


Fig. 17.21 (a) layout of the OCT system. (b) Second-generation OCT catheter-endoscope. By adjusting the angle cleaving the optical fiber and the angle polishing the GRIN lens, normal incidences are avoided and thus internal reflections can be minimized. (c) Photograph of an OCT catheter-endoscope at the distal end of the sensor. (Reprinted with permission from [57])

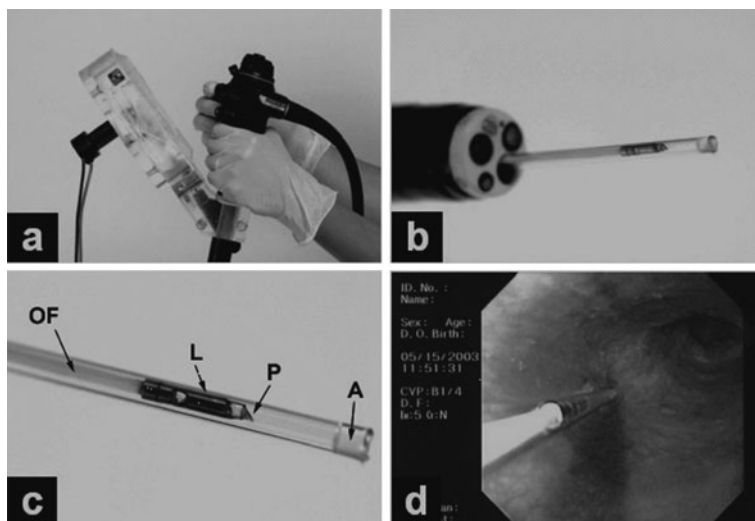


Fig. 17.22 An OCT optical fiber sensor adapted for biomedical imaging during human gastrointestinal endoscopy. (a) the proximal end of the endoscope, showing the linear translation motor that pulls the OCT fiber to-and-fro by ~ 3 mm to enable longitudinal cross-sectional imaging (b) the distal end of the endoscope, with the OCT probe protruding from the instrument channel (c) close-up of the OCT fiber sensor within its transparent sheath, with OF = optical fiber, L = focusing (GRIN) lens, P = side-reflecting prism, and A = adhesive sealant (d) clinical imaging showing OCT probe in contact with human esophageal tissue. (Reprinted with permission from [59] and [74])

A particularly important design consideration for OCT sensors is the avoidance of normal interfaces and retro-reflective surfaces, which in addition to reducing signal strength by causing photon loss, can inadvertently interfere with the reference beam and generate spurious and artificial lines or streaks in the resultant image. Thus, care must be taken to minimize the number of elements in an OCT sensor, as each one will likely contribute at least one (and often two) normal interfaces whose reflections could fall within the coherence ranging depth of the system and thus cause artifacts in the image. The use of angle-cleaved surfaces to avoid normal incidence, refractive-index matching compounds, and careful optical design to minimize the number of interfaces are thus essential for successful operation of an OCT fiber sensor. Figures 17.21(b, c) and 17.22 illustrate these concepts.

A significant limitation of OCT is its shallow imaging depth, which is typically 1–3 mm in nontransparent mammalian tissues. While a huge variety of exciting biomedical applications are still possible within this depth range (for example, endoscopic and intravascular imaging as described above, where the pathologic changes of interest occur within 1–2 mm of the inner surface), many scenarios would benefit from deep tissue imaging with OCT. Fortunately, owing to the technique's intrinsic compatibility with optical fiber technology, this can indeed be done in the context of an *interstitial* OCT fiber sensor.

Li and co-workers have first demonstrated an “OCT needle” approach suitable for deep tissue imaging in 2006 [61]. Using a single mode optical fiber with a GRIN lens and micropism to focus and deflect the beam, delivered to the desired deep tissue location via a 27-gauge needle (0.41 mm outer diameter), the authors were able to obtain high-quality microstructural images in deep-seated hamster leg muscle tissue. More recently, the Toronto OCT group [60–62] has developed interstitial probes capable of both microstructural OCT and microvascular Doppler OCT imaging in deep tissues. Using both cleaved ball lens and cleaved GRIN lens designs to minimize stray reflections as shown schematically in Fig. 17.23 and utilizing minimum footprint components, sub-mm diameter probes have been produced. X-ray or ultrasound guidance enabled accurate placement of the distal imaging end of the probe at the desired 3D location within, or at the margins, of the deep-seated tumour to be treated. While the tissue microstructure did not show obvious alterations in response to treatment (photodynamic therapy (PDT) in this case), the Doppler OCT signal changed drastically, indicating a significant treatment-induced microvascular response that can be effectively monitored both on OCT optical fiber sensors [62].

17.7 Raman Spectroscopy Fibers

17.7.1 Basic Approach

Raman spectroscopy has proven to be a valuable tool for interrogating biological materials. This technique relies on an inelastic scattering process in which incident photons transfer energy to (Stokes), or gain energy from (anti-Stokes) molecules within a sample. For biological applications, the Raman scattering accounts for approximately 10^{-10} of the incident light and the Raman signal is typically several orders of magnitude weaker than the fluorescence signal. Raman spectroscopic techniques for biomedical applications have seen significant advancement over the past few decades, with improvements in portability of equipment and fiber optic based excitation and collection, which can be used in vivo. Raman spectroscopy has been shown to provide information about the structure of molecular constituents in tissues [63, 64], and has the ability to distinguish between normal and cancerous tissues in some scenarios [65, 66].

17.7.2 Raman Probe Design

The two key parameters for designing a fiberoptic probe for Raman spectroscopy are maximizing the Raman-scattered light collection and minimizing unwanted optical signals (elastically scattered light, fluorescence photons, fiber-generated Raman signals, etc.). The intrinsically weak Raman signals can be masked by strong fluorescence from biomolecules and cells, particularly for excitation in the visible region. Fluorescence decreases rapidly at longer wavelengths, such that this problem

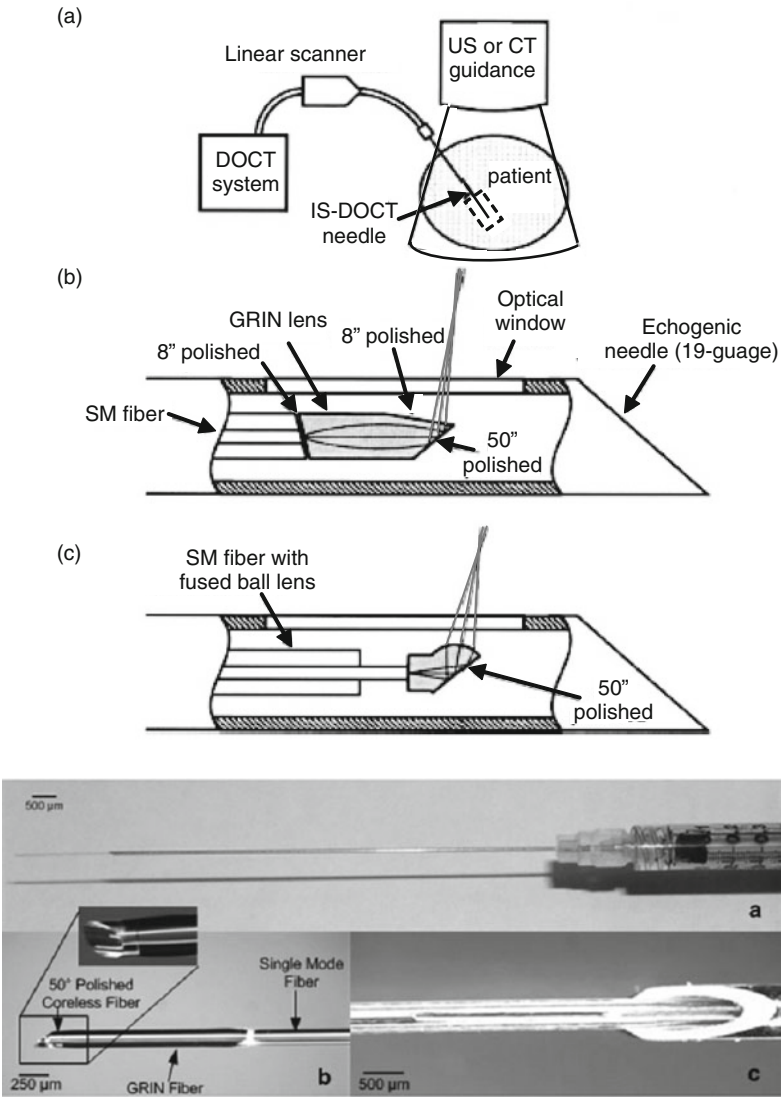


Fig. 17.23 (a) Schematic demonstrating interstitial Doppler OCT guided by either ultrasound or computed tomography (b) A beam is focused into a single mode fiber and subsequently deflected via a GRIN lens with three polished surfaces. Note the avoidance of normal interfaces in this sensor to minimize unwanted interference effects (c) Simplified schematic with a polished ball-lensed fiber. Both designs use an echogenic needle for enhanced ultrasound visualization [60]. The bottom photograph shows (d) a 2nd generation Doppler OCT needle probe used for interstitial monitoring of photodynamic therapy treatments [61]

has been largely overcome with excitation in the NIR. Alternatively, fluorescence-free Raman can be achieved with excitation in the UV below ~ 270 nm, but at the expense of reduced optical penetration (microns). For *ex vivo* tissue interrogations, integration times of a few seconds yield acceptable signal to noise ratio. For *in vivo* deployment longer integration times 20–60 s are typically required; however, the acquisition of clinical data in real-time (~ 1 s integration time) with good signal-to-noise ratios has been demonstrated for margin assessment in patients undergoing partial mastectomy [67]. Fiberoptic bundles and imaging optics can also be used to enhance collection efficiency (signal to noise), and filtering (and/or software correction) can be used to further remove unwanted signals.

Some materials used in Raman systems are themselves Raman active and hence can interfere with the signal coming from the sample under investigation. Hence, filters are required in both the delivery and collection arms of a Raman system. Fused silica fibers used to transmit optical radiation can generate Raman signals, with the intensity depending on the excitation wavelength and wavenumber region investigated. In the fingerprint region (up to ~ 2000 cm^{-1}), fused silica fibers are characterized by a strong background signal generation. These fiber-induced signals are proportional to the fiber length and can be greater than those from the sample. For high wavenumber investigations (2400 to 3800 cm^{-1}), fused silica has almost no Raman background signal. Santos et al. [68] analyzed several core, cladding and coating materials used in Raman fiber probes for investigations in the high wavenumber region. Overall, low-OH (hydroxyl) fused silica appears to be the optimal fiber material for NIR Raman applications.

One must also prevent surface reflected or elastically scattered excitation light from entering the collection fibers. This is typically achieved using a long pass filter (or notched filter) positioned in front of the collection optics. Typically a band pass filter is also used in the excitation line to allow for the transmission of only the excitation light.

A conventional Raman probe consists of a single excitation fiber and a bundle of collection fibers. Short et al. [69] developed a design with a central 200 μm excitation fiber surrounded by twenty seven 100-micron core diameter collection fibers (Fig. 17.24a). The excitation fiber can be coated, for example with gold [69] or aluminum [67], for optical isolation to prevent cross talk between the excitation and collection optics.

Haka et al. [67] developed a fiber bundle comprised of a 200- μm core diameter low OH fused silica excitation fiber (0.22 NA) surrounded by 15 collection fibers (0.27 NA) (Fig. 17.24b). The distal end of the probe contains a 0.55 mm short-pass filter rod, proximal to the excitation fiber, surrounded by a long-pass filter module positioned in front of the collection fibers. Filters are attached to the fibers using an index-matching optical cement. A 2 mm diameter sapphire ball lens (1.77 NA) is used to improve collimation of the excitation light and the collection of the Raman scattered light. The excitation fiber–lens separation determines the spot size and hence the energy density incident on the tissue. Due to the large angular distribution of the remitted Raman light, the ball lens should have a large index of refraction to improve coupling to the collection fibers.

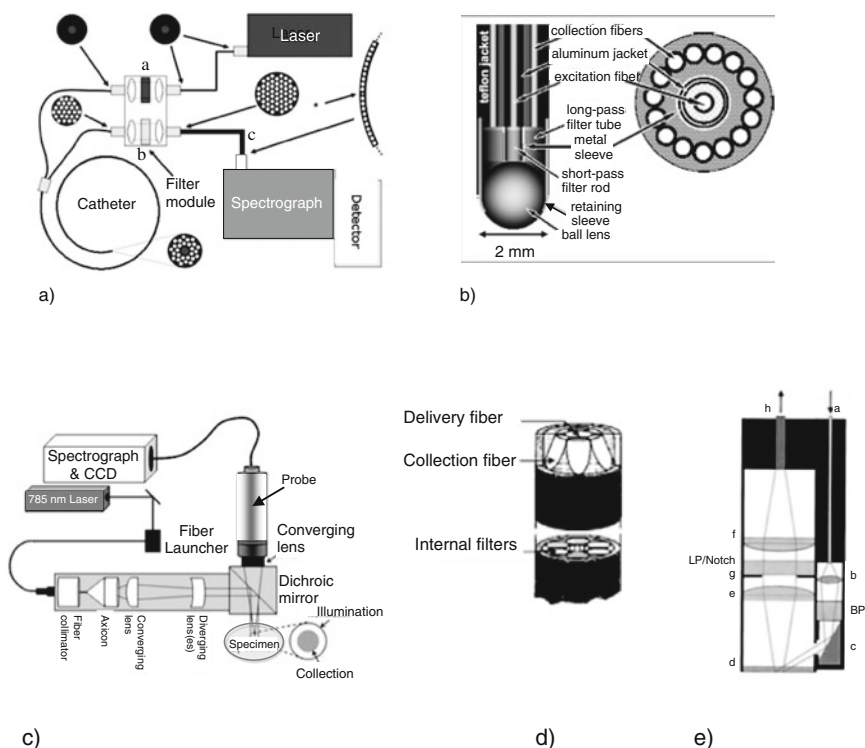


Fig. 17.24 (a) Endoscopic Raman probe based on a single illumination fiber surrounded by 27 collection fibers. Band-pass filters (label **a**) are used for the excitation fiber and long-pass filters (label **b**) for the collection fibers. A second fiber bundle consisting of 54 ultralow 100 micron core fibers is coupled to the spectrograph (label **c**) (with permission from [69]). (b) Raman probe based on a single illumination fiber surrounded by 15 collection fibers. The excitation fiber is coated with aluminum to prevent crosstalk between the excitation and collection lines. A short pass filter is used to reject background Raman signals generated in the low-OH fused silica and a long pass used on the collection line. A sapphire ball lens is used to collimate the excitation light and improve coupling of Raman light into the collection fibers (with permission from [67]). (c) Light is coupled into a 200 micron core fiber, collimated, then directed through an axon. A Galilean telescope design comprised of converging and diverging lenses is used to achieve variable ring diameters for illumination. A dichroic mirror was used to reflect excitation light to the sample and transmit collection light to a 1 mm diameter bundle of fifty 62.5 micron core fibers (with permission from [70]). (d) Endoscopic Raman probe comprised on a single central delivery fiber surrounded by seven beveled 300 micron core collection fibers. Band-pass and long-pass filters are used for the excitation and collection lines, respectively (with permission from [71]). (e) Raman probe based on excitation light, through a single 200 micron core fiber (label **a**), imaged on the tissue sample via a biconvex lens (label **b**) and mirror (label **c**). A band-pass (BP) filter is used to remove Raman background. The probe terminates in a quartz window (label **d**). Collected light is imaged using two plano convex lenses (labels **e** and **f**) through an aperture stop (label **g**) and notched filter onto a fiber bundle (label **h**) (with permission from [72])

Single point illumination can limit the amount of laser power that can be delivered due to the potential of inducing thermal damage. To overcome this, Schulmerich et al. [70] collimated light from a 200 μm core fiber directed through a 175° Axicon lens and focused using a positive-negative lens pair to create an illumination ring. Ring diameters of 3.0–14.5 mm were achieved. In this design, light is collected using a bundle of fifty 62.5- μm core diameter fibers (Fig. 17.24c).

Molckovsky et al. [71] used a fiber probe with interchangeable beveled tips (Fig. 17.24d). They demonstrated that beveled tips improved collection efficiency. Moreover, the depth of interrogation is determined by the bevel angle and separation between the central excitation fiber and surrounding seven 300- μm core diameter collection fibers. As the bevel angle is increased and separation between excitation and collection fibers is decreased, the interrogated volume moves closer to the surface. Excellent collection efficiency has been reported using this probe.

Mahadevan-Jansen et al. designed a 12 mm diameter Raman probe for cervical study (Fig. 17.24e) [72]. Light from a diode laser is coupled to a 200- μm core diameter fiber and deflected onto the tissue surface using a gold mirror. The angle of deflection is chosen such that the excitation spot overlaps with the collection region. Remitted light from the sample is collected using two biconvex lenses and imaged onto a fiber bundle consisting of fifty 100 μm core diameter fibers. The probe terminates in a quartz window, which is in contact with the tissue sample. The excitation light will induce both Raman and fluorescence photons in the quartz window, but since both processes are well known for quartz, this unwanted background signal can be identified and removed (in software). More recently, Robichaux-Viehoever et al. [73] utilized beveled collection fibers around a single excitation to achieve overlap of the excitation and collection regions.

For medical applications, Raman fiber probe design must also address a number of clinical considerations. Practical probe dimensions are typically up to 2 mm (diameter) to allow for insertion into needles and endoscopes, and fiber lengths can be on the order of a few meters.

17.8 Summary

Optical fiber sensors offer unique capabilities for accurate assessment of biological tissues, with interesting applications towards early disease diagnosis, therapy guidance and feedback, and treatment response monitoring. Depending on a particular clinical application and intent, they may be advantageous due to their bio-compatibility, freedom from electromagnetic interference, choice of technological design parameters that may be individually optimized, and ability to furnish a variety of useful tissue characterization information that may be difficult/impossible to obtain by other means. The overview presented in this chapter has discussed basic operating principles of fiber sensors, reviewed the types of fibers currently employed in biomedicine, and provided illustrative examples of their biomedical

use. It is hoped that the presented concepts and applications of optical fiber sensors convey the scope of the basic science, enabling technology, and useful approaches and innovations that are occurring in this exciting field.

Acknowledgement The authors would like to thank Dr. Richard Schwarz from the Richards-Kortum lab at The University of Texas at Austin for providing the derivation of the ball-lens equation.

References

1. Kapany NS. *Fiber optics. Principles and applications*. Academic, New York (1967).
2. Utzinger U and Richards-Kortum RR. Fiber optic probes for biomedical optical spectroscopy. *J. Biomed. Opt.*, 8(1):121–147 (2003).
3. Verdaasdonk RM and Borst C. Optics of fiber and fiber probes. In: AJ Welch and MJC van Gemert (eds) *Optical-thermal response of laser-irradiated tissue*. Plenum, New York, pp. 619–666 (1995).
4. Polymicro Technologies Catalog, http://www.polymicro.com/catalog/2_8.htm (2009).
5. Chin LC, Wilson BC, Whelan WM, and Vitkin IA. Radiance-based monitoring of the extent of tissue coagulation during laser interstitial thermal therapy. *Opt. Lett.*, 29(9):959–961 (2004).
6. Dickey DJ, Moore RB, Rayner DC, and Tulip J. Light dosimetry using the P3 approximation. *Phys. Med. Biol.*, 46(9):2359–2370 (2001).
7. Farrell TJ, Patterson MS, and Wilson BC. A diffusion theory model of spatially, resolved, steady-state diffuse reflectance for the non-invasive determination of tissue optical properties in vivo. *Med. Phys.*, 19:879–888 (1992).
8. Hull EL, Nichols MG, and Foster TH. Quantitative broadband near-infrared spectroscopy of tissue-simulating phantoms containing erythrocytes. *Phys. Med. Biol.*, 43(11):3381–3404 (1998).
9. Wang L and Jacques SL. Use of a laser beam with an oblique angle of incidence to measure the reduced scattering coefficient of a medium. *Appl. Opt.*, 34(13):2362–2366 (1995).
10. Nichols MG, Hull EL, and Foster TH. Design and testing of a white-light, steady-state reflectance spectrometer for determination of optical properties of highly scattering systems. *Appl. Opt.*, 36(1):93–104 (1997).
11. Fuchs H, Utzinger U, Zuluaga F, Gillenwater R, Jacob R, Kemp B, and Richards-Kortum R. Combined fluorescence and reflectance spectroscopy: in vivo assessment of oral cavity epithelial neoplasia. *Proc. CLEO*, 6:306–307 (1998).
12. Patterson MS, Andersson-Engels S, Wilson BC, and Osei EK. Absorption spectroscopy in tissue-simulating materials: a theoretical and experimental study of photon paths. *Appl. Opt.*, 34(1):22–30 (1995).
13. Farrell TJ, Patterson MS, and Wilson B. A diffusion theory model of spatially resolved, steady-state diffuse reflectance for the noninvasive determination of tissue optical properties in vivo. *Med. Phys.*, 19(4):879–888 (1992).
14. Finlay JC and Foster TH. Hemoglobin oxygen saturations in phantoms and in vivo from measurements of steady-state diffuse reflectance at a single, short source-detector separation. *Med. Phys.*, 31(7):1949–1959 (2004).
15. Seo I, Hayakawa CK, and Venugopalan V. Radiative transport in the delta-P1 approximation for semi-infinite turbid media. *Med. Phys.*, 35(2):681–693 (2008).
16. Kienle A and Patterson MS. Determination of the optical properties of turbid media from a single Monte Carlo simulation. *Phys. Med. Biol.*, 41(10):2221–2227 (1996).
17. Kim AD, Hayakawa C, and Venugopalan V. Estimating optical properties in layered tissues by use of the Born approximation of the radiative transport equation. *Opt. Lett.*, 31(8):1088–1090 (2006).

18. Pfefer TJ, Matchette LS, Bennett CL, Gall JA, Wilke JN, Durkin AJ, and Ediger MN. Reflectance-based determination of optical properties in highly attenuating tissue. *J. Biomed. Opt.*, 8(2):206–215 (2003).
19. Alexandrakis G, Farrell TJ, and Patterson MS. Monte carlo diffusion hybrid model for photon migration in a two-layer turbid medium in the frequency domain. *Appl. Opt.*, 39(13):2235–2244 (2000).
20. Seo I, You JS, Hayakawa CK, and Venugopalan V. Perturbation and differential Monte Carlo methods for measurement of optical properties in a layered epithelial tissue model. *J. Biomed. Opt.*, 12(1):014030 (2007).
21. Mourant JR, Bigio IJ, Jack DA, Johnson TM, and Miller HD. Measuring absorption coefficients in small volumes of highly scattering media: Source-detector separations for which path lengths do not depend on scattering properties. *Appl. Opt.*, 36(22):5655–5661 (1997).
22. Kumar G and Schmitt JM. Optimal probe geometry for near-infrared spectroscopy of biological tissue. *Appl. Opt.*, 36(10):2286–2293 (1997).
23. Amelink A, Kaspers OP, Sterenborg HJ, van der Wal JE, Roodenburg JL, and Witjes MJ. Non-invasive measurement of the morphology and physiology of oral mucosa by use of optical spectroscopy. *Oral. Oncol.*, 44(1):65–71 (2008).
24. Van de Hulst HC. *Light scattering by small particles*. Dover, New York (1957).
25. van Veen RL, Amelink A, Menke-Pluymers M, van der Pol C, and Sterenborg HJ. Optical biopsy of breast tissue using differential path-length spectroscopy. *Phys. Med. Biol.*, 50(11):2573–2581 (2005).
26. Amelink A, OP Kaspers, HJCM Sterenborg, JE van der Wal, JLN Roodenburg, and MJH Witjes. Non-invasive measurement of the morphology and physiology of oral mucosa by use of optical spectroscopy. *Oral Oncol.*, 44:65–71 (2008).
27. Kruijt B, de Bruijn HS, van der Ploeg-van den Heuvel A, de Bruin RW, Sterenborg HJ, Amelink A, and Robinson DJ. Monitoring ALA-induced PpIX photodynamic therapy in the rat esophagus using fluorescence and reflectance spectroscopy. *Photochem. Photobiol.*, 6:1515–1527 (2008).
28. Wang AMJ, Bender JE, Pfefer J, Utzinger U, and Drezek RA. Depth-sensitive reflectance measurements using obliquely oriented fiber probes. *J. Biomed. Opt.*, 10(4):044017 (2005).
29. Arifler D, Schwarz RA, Chang SK, and Richards-Kortum R. Reflectance spectroscopy for diagnosis of epithelial precancer: model-based analysis of fiber-optic probe designs to resolve spectral information from epithelium and stroma. *Appl. Opt.*, 44(20):4291–4305 (2005).
30. Nieman L, Myakov A, Aaron J, and Sokolov K. Optical sectioning using a fiber probe with an angled illumination-collection geometry: evaluation in engineered tissue phantom. *Appl. Opt.*, 43:1308–1319 (2004).
31. Skala M, Palmer G, Zhu C, Liu Q, Vrotsos K, Marshek-Stone C, Gendron-Fitzpatrick A, and Ramanujam N. Investigation of the fiber-optic probe designs for optical spectroscopic diagnosis of epithelial pre-cancers. *Lasers Surg. Med.*, 34:25–38 (2004).
32. Schwarz RA, Arifler D, Chang SK, Pavlova I, Hussain IA, Mack V, Knight B, Richards-Kortum R, and Gillenwater AM. Ball lens coupled fiber-optic probe for depth-resolved spectroscopy of epithelial tissue. *Opt. Lett.*, 30(10):1159–1161 (2005).
33. Schwarz RA, Gao W, Daye D, Williams MD, Richards-Kortum R, and Gillenwater AM. Autofluorescence and diffuse reflectance spectroscopy of oral epithelial tissue using a depth-sensitive fiber-optic probe. *Appl. Opt.*, 47(6):825–834 (2008).
34. Johnson T and Mourant J. Polarized wavelength-dependent measurements of turbid media. *Opt. Express*, 4(6):200–216 (1999).
35. Myakov A, Nieman L, Wicky L, Utzinger U, Richards-Kortum R, and Sokolov K. Fiber optic probe for polarized reflectance spectroscopy in vivo: design and performance. *J. Biomed. Opt.*, 7(3):388–397 (2002).
36. Groner W, Winkelman JW, Harris AG, Ince C, Bouma GJ, Messmer K, and Nadeau RG. Orthogonal polarization spectral imaging: a new method for study of the microcirculation. *Nat. Med.*, 5(10):1209–1213 (1999).

37. De Jode ML. Monte Carlo simulations of the use of isotropic light dosimetry probes to monitor energy fluence in biological tissues. *Phys. Med. Biol.*, 44:3207–3237 (1999).
38. Henderson B. *An isotropic dosimetry probe for monitoring light in tissue, theoretical and experimental measurement*. Ph.D. Thesis, Heriot Watt University, Edinburgh (1991).
39. Marijnissen JP, Star WM. Calibration of isotropic light dosimetry probes based on scattering bulbs in clear media. *Phys. Med. Biol.*, 41(7):1191–1208 (1996).
40. Marijnissen JP and Star WM. Performance of isotropic light dosimetry probes based on scattering bulbs in turbid media. *Phys. Med. Biol.*, 47(12):2049–2058 (2002).
41. Lilge L, Haw T, and Wilson BC. Miniature isotropic optical fibre probes for quantitative light dosimetry in tissue. *Phys. Med. Biol.*, 38(2):215–230 (1993).
42. Dimofte A, Finlay JC, and Zhu TC. A method for determination of the absorption and scattering properties interstitially in turbid media. *Phys. Med. Biol.*, 50(10):2291–2311 (2005).
43. Pomerleau-Dalcourt N and Lilge L. Development and characterization of multi-sensory fluence rate probes. *Phys. Med. Biol.*, 51(7):1929–1940 (2006).
44. Richards-Kortum R. Fluorescence spectroscopy of turbid media. In: AJ Welch and MJC van Gemert (eds) *Optical thermal response of laser-irradiated tissue*. Plenum, New York, pp. 667–706 (1995).
45. Zhu C, Liu Quan, Ramanujam N. Effect of fiber optic probe geometry on depth-resolved fluorescence measurements from epithelial tissues: a Monte Carlo simulation. *J. Biomed. Opt.*, 8(2), 237–247 (2003).
46. Trujillo EV, Sandison DR, Utzinger U, Ramanujam N, Mitchell MF, and Richard-Kortum R. Method to determine tissue fluorescence efficiency in vivo and predict signal-to-noise for spectrometers. *Appl. Spectrosc.*, 52(7):943–995 (1998).
47. Pope K, Warren S, Yazdi Y, Johnston J, David M, and Richard-Kortum R. Dual imaging of arterial walls: intravascular ultrasound and fluorescence spectroscopy. *Proc. SPIE*, 1878:42–50 (1993).
48. Pfefer TJ, Schomacker KT, Ediger MN, and Nishioka NS. Multiple-fiber probe design for fluorescence spectroscopy in tissue. *Appl. Opt.*, 41(22):4712–4721 (2002).
49. Keijzer M, Richards-Kortum R, Jacques SL, and Feld MS. Fluorescence spectroscopy of turbid media: Autofluorescence of the human aorta. *Appl. Opt.*, 28:4286–4292 (1989).
50. Avrillier S, Tinet D, Ettori D, Tualle JM, and Gelebart B. Influence of the emission reception geometry in laser-induced fluorescence spectra from turbid media. *Appl. Opt.*, 37:2781–2787 (1998).
51. Gardner CM, Jacques SL, Welch AJ. Fluorescence spectroscopy of tissue: Recovery of intrinsic fluorescence from measured fluorescence. *Appl. Opt.*, 35:1780–1792 (1996).
52. Gardner CM, Jacques SL, Welch AJ. Light transport in tissue: accurate expressions for one-dimensional fluence rate and escape function based upon Monte Carlo simulation. *Lasers Surg. Med.*, 18:129–138 (1996).
53. Durkin AJ, Richards-Kortum R. Comparison of methods to determine chromophore concentrations from fluorescence spectra of turbid samples. *Lasers Surg. Med.*, 19:75–89 (1996).
54. Finlay JC, Conover DL, Hull EL, Foster TH. Porphyrin bleaching and PDT-induced spectral changes are irradiance dependent in ALA-sensitized normal rat skin *in vivo*. *Photochem. Photobiol.*, 73:54–63 (2001).
55. Wu J, Feld MS, and Rava R. Analytical model for extracting intrinsic fluorescence in turbid media. *Appl. Opt.*, 32:3583–3595 (1993).
56. Finlay JC and Foster TH. Recovery of hemoglobin oxygen saturation and intrinsic fluorescence with a forward-adjoint model. *Appl. Opt.*, 44(10):1917–1933 (2005).
57. Tearney GJ, Brezinski ME, Bouma BE, Boppart SA, Pitris C, Southern JF, and Fujimoto JG. In vivo endoscopic optical biopsy with optical coherence tomography. *Science*, 276:2037–2039 (1997).

58. Kawasaki M, Bouma B, Bressner J, Houser S, Nadkarni S, MacNeill B, Jang I, Fujiwara H, and Tearney G. Diagnostic accuracy of optical coherence tomography and integrated backscatter intravascular ultrasound images for tissue characterization of human coronary plaques. *J. Am. Coll. Cardiol.*, 48:81–88 (2006).
59. Yang SJ, Marcon N, Gardiner G, Qi B, Bisland S, Seng-Yue E, Lo S, Pekar J, Wilson B, and Vitkin I. High speed, wide velocity dynamic range Doppler optical coherence tomography (Part III): in vivo endoscopic imaging of blood flow in the rat and human gastrointestinal tracts. *Opt. Express*, 11(19):2416–2424 (2003).
60. Yang VX, Mao YX, Munce N, Standish B, Kucharczyk W, Marcon NE, Wilson BC, and Vitkin IA. Interstitial Doppler optical coherence tomography. *Opt. Lett.*, 30(14):1791–1793 (2005).
61. Li H, Standish BA, Mariampillai A, Munce NR, Mao Y, Chiu S, Marcon NE, Wilson BC, Vitkin A, and Yang VX. Feasibility of interstitial Doppler optical coherence tomography for in vivo detection of microvascular changes during photodynamic therapy. *Lasers Surg. Med.*, 38(8):754–761 (2006).
62. Standish BA, Lee KK, Jin X, Mariampillai A, Munce NR, Wood MF, Wilson BC, Vitkin IA, and Yang VX. Interstitial Doppler optical coherence tomography as a local tumor necrosis predictor in photodynamic therapy of prostatic carcinoma: An in vivo study. *Cancer Res.*, 68(23):9987–9995 (2008).
63. De Jong BWD, Schut TCB, Wolffenbuttel KP, Nijman JM, Kok DJ, and Puppels GJ. Identification of bladder wall layers by Raman spectroscopy. *J. Urol.*, 168:1771–1778 (2002).
64. Nottingher I, Verrier S, Romanska H, Bishop AE, Polak JM, and Hench LL. *In situ* characterization of living cells by Raman spectroscopy. *Spectroscopy*, 16:43–51 (2002).
65. Mahadevan-Jansen A and Richards-Kortum R. Raman spectroscopy for the detection of cancers and precancers. *J. Biomed. Opt.*, 1:31–70 (1996).
66. Haka AS, Shafer-Peltier KE, Fitzmaurice M, Crowe J, Dasari RR, and Feld MS. Diagnosing breast cancer by using Raman spectroscopy. *Proc. Natl. Acad. Sci. U.S.A.*, 102:12371–12376 (2005).
67. Haka AVolynskaya, Z, Gardecki J, Nazemi J, Lyons J, Hicks D, Fitzmaurice M, Dasri R, Crowe J, and Felds M. In vivo margin assessment during partial mastectomy breast surgery using Raman spectroscopy. *Cancer Res.*, 66:3317–3322 (2006).
68. Santos LF, Wolthuis R, Koljenović S, Almeida RM, and Puppels GJ. Fiber-optic probes for in vivo Raman spectroscopy in the high-wavenumber region. *Anal. Chem.*, 77(20):6747–6752 (2005).
69. Short M, Lam S, McWilliams A, Zhao J, and Lui Hand Zeng H. Development and preliminary results of an endoscopic probe for potential in vivo diagnosis of lung cancers. *Opt. Lett.*, 33:711–713 (2008).
70. Schulmerich MV, Dooley KA, Morris MD, Vanasse TM, and Goldstein SA. Transcutaneous fiber optic raman spectroscopy of bone using annular illumination and a circular array of collection fibers. *J. Biomed. Opt.*, 11(6):060502 (2006).
71. Molckovsky A, Wong Kee Song LM, Shim MG, Marcon NE, and Wilson BC. Diagnostic potential of near infrared Raman spectroscopy of the colon: Differentiating adenomatous from hyperplastic polyps. *Gastrointestinal Endosc.*, 57:396–402 (2003).
72. Mahadevan-Jansen A, Mitchell MF, Ramanujam N, Utzinger U, and Richards-Kortum R. Development of a fiber optic probe to measure NIR Raman spectra of cervical tissue *in vivo*. *Photochem. Photobiol.*, 683:427–431 (1998).
73. Robichaux-Viehoever A, Kanter E, Shappell H, Billheimer D, Jones H III, and Mahadevan-Jansen A. Characterization of Raman spectra measured in vivo for the detection of cervical dysplasia. *Appl. Spectrosc.*, 61(9):986–993 (2007).
74. Victor XD, Tang YS, Gordon ML, Qi B, Gardiner G, Cirocco M, Kortan P, Haber GB, Kandel G, Vitkin IA, Wilson BC, and Marcon NE. Endoscopic Doppler optical coherence tomography in the human GI tract: Initial experience. *GI Endosc.*, 61(7):879–890 (2005).